Ocean Engineering 330 (2025) 121301

Contents lists available at ScienceDirect

Ocean Engineering

journal homepage: www.elsevier.com/locate/oceaneng

Research paper

Analysis and active control of vortex-induced vibration of hydrofoil

Jinliang Wu [a], Pengxiang Zhao [a], Xin Lan [b], Jinsong Leng [b,**], Yanju Liu [a,*]

[a] Department of Astronautical Science and Mechanics, Harbin Institute of Technology (HIT), P.O. Box 301, No. 92 West Dazhi Street, Harbin, 150001, People's Republic of China

[b] Center for Composite Materials and Structures, Harbin Institute of Technology (HIT), No. 2 YiKuang Street, Harbin, 150080, People's Republic of China

ARTICLE INFO

Keywords:
Fluid-structure coupling
Vortex-induced vibration
Vortex shedding
Active control

ABSTRACT

Vortex-induced vibration (VIV) of hydrofoils poses significant challenges to underwater equipment and marine engineering, involving the coordinated optimization of structural safety and acoustic performance. This study proposes an active control strategy based on piezoelectric materials to effectively suppress vibration and noise through vortex shedding frequency modulation under fluid-structure interaction conditions. By establishing a bidirectional fluid-structure coupling simulation model, we systematically investigated the torsional vibration response and resonance mechanisms of hydrofoils under various flow velocities, revealing dynamic influence patterns of velocity variations on wake vortex shedding and acoustic field characteristics. The mechanism of active control on structural vibration energy dissipation and flow field pressure distribution was elucidated through excitation amplitude and frequency regulation. Experimental studies employing Macro Fiber Composite (MFC) and particle image velocimetry (PIV) validated the active modulation characteristics of wake vortex shedding. Results demonstrate that piezoelectric excitation can significantly alter boundary layer evolution on hydrofoil surfaces, adjust vortex shedding frequencies, mitigate resonance risks, and optimize acoustic field distribution. This research provides a novel technical approach for vibration control in complex fluid-structure coupling systems and active acoustic signature regulation.

1. Introduction

Hydrofoil is an important component of marine wing, which is widely used in ships. In addition to the main function of providing lift, it can also be designed in different forms to improve the stability and maneuverability of the ship. It is widely used in ships and some hydraulic machinery. In the use of underwater equipment and ocean engineering, the vortex-induced vibration of hydrofoils is a significant phenomenon. When the fluid flows through the hydrofoil, the unsteady hydrodynamic force will be exerted on the hydrofoil by alternating vortices falling off at the back, resulting in structural vibration. Resonance will occur and the hydrofoil's amplitude will greatly rise as its vortex shedding frequency approaches its natural frequency. Resonance can cause structural damage to equipment, such as ship propellers (Lee et al., 2016; Tian et al., 2017), pump (Kang et al., 2022), water turbine (Zobeiri et al., 2012) and wave glider (Zhang et al., 2022). In addition, the interaction of propeller vortex shedding with its natural frequency leads to singing (Kim et al., 2020; Wang et al., 2022). In recent years, composite materials have been used more and more in practical engineering because of their advantages such as light weight. When an unstable flow passes over a light and flexible hydrofoil, the interaction of the vortex with the trailing edge falling off and structural vibration becomes more significant (Lee et al., 2016). As a result, analyzing the vortex-induced vibration characteristics of hydrofoils under various working situations, as well as controlling or regulating the vortex-induced vibration of hydrofoils, is critical for underwater equipment and ocean engineering applications.

When the fluid flows through the structure, with the change of velocity, it will form a periodic shedding vortex behind the structure. In recent decades, the development process of alternate shedding vortices has been thoroughly investigated (Green and Gerrard, 1993; Griffin, 1995). The findings demonstrate that the upper and bottom surfaces of the structure split from one another as a result of the interaction between the shear layers on its surface and that these surfaces subsequently manifest as vortex in the wake. Alternating shedding vortices may cause structural vibrations (Khalak and Williamson, 1999). Resonance will also happen when the vortex shedding frequency is near the structure's natural frequency (Bearman, 2003; Feng, 1968). Williamson and Roshko

* Corresponding author.
** Corresponding author.
E-mail addresses: lengjs@hit.edu.cn (J. Leng), yj_liu@hit.edu.cn (Y. Liu).

https://doi.org/10.1016/j.oceaneng.2025.121301
Received 3 January 2025; Received in revised form 7 April 2025; Accepted 17 April 2025
Available online 21 April 2025

(1988) analyzed the vortex mode of the cylinder under different flow rates and compared and analyzed the reasons for the change of the vortex shedding mode. Griffin (1995) conducted an experimental study on the shedding of cylindrical wake vortex at low Reynolds number and compared and analyzed the process of vortex generation.

The hydrofoil construction is then widely employed in ocean engineering and undersea equipment. Numerous studies have been conducted on the hydrofoil's vortex-induced vibration mechanism. Hu et al. (2022) used the SST $k-\omega$ model of shear application transport to carry out fluid-structure coupling simulation calculation for three-dimensional hydrofoil. The vibration characteristics and flow field changes of three-dimensional hydrofoil fluid-structure coupling are studied. Yarusevych and H. Boutilier (2011) conducted an experimental study on boundary layer separation of hydrofoil at low Reynolds number at 10° angle of attack. The study found that when the Reynolds number is less than 7×10^4, foil surface form vortex shear layer without separation. When the Reynolds number is greater than 1×10^5, a periodic shedding vortex is formed. Ni et al. (2019) conducted a slot on the hydrofoil and analyzed the lift resistance characteristics of the hydrofoil through simulation and experiment, Dongyang et al. (2023b) found that cylinder vibrations can significantly alter the aerodynamic characteristics of airfoils. The outcomes demonstrate that slotting can successfully enhance hydrofoil performance. In addition, the vibration characteristics of hydrofoil are also studied. For example, transition of hydrofoil boundary layer affects hydrofoil vibration (Ducoin et al., 2012), structural vibration caused by the shedding of hydrofoil trailing edge vortex (Smith et al., 2021), and fluid-structure coupling affects the cavitation of flexible hydrofoil (Smith et al., 2020; Young et al., 2022).

With further study, the frequency-locking phenomenon of hydrofoil was also found (Hartmann et al., 2013). An experimental investigation on the vortex-induced vibration of airfoils was carried out by Kamrass et al. (2016). It is discovered that the highest vibration response occurs when the vortex shedding frequency remains close to the natural frequency. Qin et al. (2023) analyzed elastic hydrofoils with various trailing edge incisions using vortex-induced vibration simulation. We compare and examine the frequency locking under various natural frequencies. The impact of the trailing edge's cutting angle on hydrofoil vibration is examined. The optimum cutting angle of trailing edge for reducing hydrofoil vibration is determined, and the reason for the small vibration is analyzed. Zhao et al. (2024a) simulated and analyzed the change of active vibration hydrofoil vortex shedding based on the wake oscillation model. It is found that by varying the vibration frequency and amplitude, the vortex's shedding frequency may be locked with the structure's vibration frequency.

Recent research focuses on the vibration control of hydrofoil by various means. Nonlinear energy regulation technologies demonstrate unique potential in VIV control. For instance, Dongyang et al. (2023a) proposed a fluid-structure interaction control strategy based on a Nonlinear Energy Sink (NES), which suppresses vibrations by targeted dissipation of vortex-induced energy. Similarly, Zhang et al. (2024a) investigated VIV characteristics in rigidly connected multi-cylinder systems, revealing that nonlinear spring mechanisms can broaden lock-in frequency ranges but struggle to concurrently mitigate high-frequency noise. These studies indicate that passive nonlinear control methods, while alleviating resonance, inherently lack dynamic adaptability. In contrast, active control strategies overcome the bandwidth limitations of passive approaches through real-time modulation of external excitation parameters (Zhang et al., 2024b). Inspired by these advances, this work pioneers the integration of bidirectional fluid-structure coupling with piezoelectric active control to dynamically regulate hydrofoil vortex shedding frequencies, thereby achieving targeted suppression of torsional vibrations.

Piezoelectric materials have attracted wide attention due to their unique mechanoelectric coupling properties (Caverly et al., 2016; Mehmood et al., 2012; Muddada and Patnaik, 2010). By putting a little

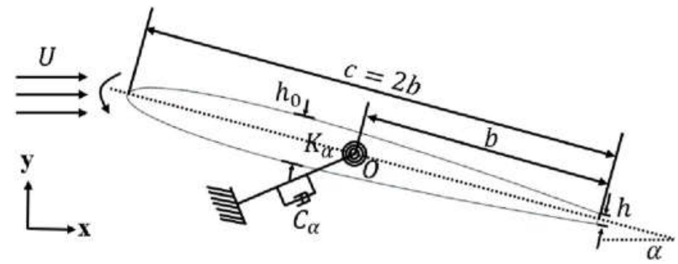

Fig. 1. Pitch motion of a hydrofoil with one degree of freedom.

perturbation of piezoelectric ceramics on the blunt body's surface, L. Cheng (2003) modify the interplay between vortex shedding and vortex-induced vibration of a blunt body. Shigeki et al. (2018) used a twin-wafer piezoelectric actuator to confirm the efficacy of master control of vortex-induced vibration. Hasheminejad and Masoumi (2022) established a feedback control model using piezoelectric actuators to actively control the vortex-induced vibration of an elastic cylinder in laminar flow. The results show that this method can effectively control the fluctuation of lift and drag coefficients and realize the rapid attenuation of motion. Zhao et al. (2024b) established an active control model of hydrofoil vortex-induced vibration by applying a high-stiffness piezoelectric actuator, and applied the FxLMS control algorithm to actively control hydrofoil vortex-induced vibration. Although piezoelectric materials have been used in the field of hydrofoil vibration control, the active control based on bidirectional fluid-structure coupling is less studied. The innovation of this study is manifested in two aspects: (1) Methodological innovation: The application of user-defined function (UDF) in ANSYS Fluent enables precise simulation of hydrofoil torsional vibrations and implements active open-loop control, achieving dynamic coupling of fluid-structure interaction and actuator response. (2) Engineering application innovation: Experimental validation confirms the capability to regulate vortex shedding frequencies in hydrofoil simulations, providing a novel solution for active acoustic signature modulation of underwater structures such as marine propellers. This approach bridges the gap between numerical predictions and practical noise control requirements in marine engineering.

This research investigates the relationship between vortex shedding and vortex-induced vibrations (VIV) in hydrofoils, aiming to achieve active regulation of hydrofoil VIV. The paper is structured as follows: Section 2 establishes a simulation framework for active VIV control of hydrofoils based on a bidirectional fluid-structure coupling model, detailing the governing equations, mesh generation strategies, and dynamic boundary condition configurations. Section 3 validates the numerical model's reliability through grid independence verification and experimental benchmarking. Section 4 investigates the effects of excitation amplitudes and frequencies on hydrofoil torsional vibrations via systematic numerical simulations. Section 5 demonstrates the tunability of vortex shedding frequencies through PIV experiments combined with MFC active actuation. Section 6 summarizes the key findings and highlights the methodological innovations.

2. Simulation of hydrofoil vortex-induced vibration active control

2.1. Geometric model

The two-dimensional NACA0009 hydrofoil with a truncated trailing edge is investigated. A spring with one pitching motion degree is used to support the hydrofoil. The airfoil is identical to Ausoni et al. (2006)'s experimental model. The hydrofoil's maximum thickness is $h_0 = 0.09c_0$, and its initial chord length is $c_0 = 0.11m$. The truncated hydrofoil chord length is $c = 2b = 0.1m$ and the trailing edge thickness is $h = 3.22 \times$

$10^{-3}m$, as shown in Fig. 1. The center O of the pitching motion is b from the leading edge, the initial angle of attack is 0°, and the angle α of the pitching motion is defined as positive in the clockwise direction. The fluid medium is water, the dimensionless reduced velocity $U_r = U/(f_{vs} \times h)$, where U is the incoming flow velocity, f_{vs} is the vortex emitting frequency.

2.2. Mathematical model

2.2.1. CFD simulation

For incompressible uniform flow, the governing equations are expressed in Cartesian coordinates as follows:

$$\frac{\partial u_i}{\partial t} + u_j\frac{\partial u_i}{\partial x_j} = -\frac{1}{\rho}\frac{\partial p}{\partial x_i} + \nu\frac{\partial^2 u_i}{\partial x_i \partial x_j} + f_i, i = 1, 2, 3 \tag{1}$$

$$\frac{\partial u_i}{\partial x_i} = 0, i = 1, 2, 3 \tag{2}$$

where ρ is the fluid density, ν is the kinematic viscosity coefficient, f_i represents the body force components, with $i = 1, 2, 3$ referring to the three degrees of freedom.

The Shear Stress Transport $SSTk-\omega$ turbulence model is employed for numerical simulations. The governing equations for the $SSTk-\omega$ model are:

$$\frac{\partial(\rho k)}{\partial t} + \nabla\cdot(\rho k\overline{u}) = \nabla\cdot\left[\left(\mu + \frac{\mu_t}{\sigma_k}\right)\nabla k\right] + G_k - Y_k + S_k \tag{3}$$

$$\frac{\partial(\rho\omega)}{\partial t} + \nabla\cdot(\rho\omega\overline{u}) = \nabla\cdot\left[\left(\mu + \frac{\mu_t}{\sigma_\omega}\right)\nabla\omega\right] + G_\omega - Y_\omega + S_\omega \tag{4}$$

where G_k and G_ω denote the production of turbulent kinetic energy k and the specific dissipation rate ω , respectively. Likewise, E_k and E_ω denote their effective diffusivity, and σ_k and σ_ω denote their turbulent Prandtl numbers. μ_t is the turbulent viscosity. D_ω is the diffusion part of the equation. S_k and S_ω are customized items.

In computational fluid dynamics, transition models are employed to predict the onset location of laminar-to-turbulent transition in flow fields. Compared with the $\gamma - \mathrm{Re}_\theta$ transition model, the γ intermittency transition model adopted in this study requires only solving the transport equation for turbulent intermittency factor γ, expressed as:

$$\frac{\partial(\rho\gamma)}{\partial t} + \nabla\cdot(\rho\overline{u}\gamma) = \nabla\cdot\left[\left(\mu + \frac{\mu_t}{\sigma_\gamma}\right)\nabla\gamma\right] + P_\gamma - E_\gamma \tag{5}$$

where, P_γ denotes the destruction source term while E_γ represents the transition source term.

This transition modeling framework achieves accurate boundary layer flow characterization through coupling with the $SSTk-\omega$ turbulence model. Specifically, the coupling mechanism implements modifications to both the turbulent kinetic energy production term G_k and dissipation term Y_k in Equation (3):

$$G_k^* = \gamma_{eff} G_k \tag{6}$$

$$Y_k^* = \min\left\{\max\left(\gamma_{eff}, 0.1\right), 0.1\right\} Y_k \tag{7}$$

where γ_{eff} signifies the intermittency factor correction term. The proposed coupled methodology demonstrates enhanced capability in simulating the laminar-turbulent transition process over hydrodynamically smooth hydrofoils.

2.2.2. Underwater acoustic model

The acoustic analogy proposed by Lighthill and extended by Ffowcs Williams and Hawkings (FW-H equation) is adopted to model hydrodynamic noise generation. The equation is based on an integral representation of the area over the source distribution in the acoustic field to predict the noise generated by unsteady flow, which can be derived from the continuity and energy equations of the flow. The FW-H equation is formulated as:

$$\frac{1}{a_0^2}\frac{\partial^2 p'}{\partial t^2} - \nabla^2 p' = \frac{\partial^2\Omega}{\partial x_i \partial x_j}\left\{T_{ij}H(f)\right\} - \frac{\partial}{\partial x_i}\left\{\left[P_{ij}n_j + \rho u_i(u_n - v_n)\right]\delta(f)\right\} + \frac{\partial}{\partial t}\left\{\left[\rho_0 v_n + \rho(u_n - v_n)\right]\delta(f)\right\} \tag{8}$$

where i denotes the direction along coordinate x_i, n denotes the direction normal to the surface $f = 0$, u denotes the fluid velocity, v denotes the surface velocity, $\delta(f)$ is the Dirac function, and $H(f)$ is the Heaviside function. a_0 is the far-field sound velocity, P_{ij} is the compressive stress tensor, and T_{ij} is the Lighthill stress tensor. The far-field acoustic pressure p' comprises thickness noise $p'_T(x,t)$ and loading noise $p'_L(x,t)$:

$$p'(x,t) = p'_T(x,t) + p'_L(x,t) \tag{9}$$

Thickness noise and loading noise are defined as:

$$4\pi p'_T(x,t) = \int_{f=0}\left[\frac{\rho_0(\dot{U}_n + U_n)}{r(1-M_r)^2}\right]dS + \int_{f=0}\left[\frac{\rho_0 U_n\left(r\dot{M}_r + a_0\left(M_r - M^2\right)\right)}{r^2(1-M_r)^3}\right]dS \tag{10}$$

$$4\pi p'_L(x,t) = \int_{f=0}\left[\frac{\dot{L}_r}{r(1-M_r)^2}\right]dS + \int_{f=0}\left[\frac{L_r - L_M}{r^2(1-M_r)^2}\right]dS + \frac{1}{a_0}\int_{f=0}\left[\frac{L_r\left(r\dot{M}_r + a_0\left(M_r - M^2\right)\right)}{r^2(1-M_r)^3}\right]_{ret} dS \tag{11}$$

where

$$U_n = \left(v_i + \frac{\rho}{\rho_0}(u_i - v_i)\right)n_i \tag{12}$$

$$L_r = \left(P_{ij}\widehat{n}_j + \rho u_i(u_n - v_n)\right)r_i \tag{13}$$

$$L_M = \left(P_{ij}\widehat{n}_j + \rho u_i(u_n - v_n)\right)\frac{v_i}{a_0} \tag{14}$$

$$M_r = \frac{v_i}{a_0}r_i \tag{15}$$

where x represents the receiver's position, t is the observer time. ρ_0 is the density of incompressible flow, ρ is the density of compressible flow. r_i and n_i denote the unit vectors in the radiation and wall-normal directions, respectively. The dot over a variable denotes source-time differentiation of that variable.

The sound pressure level (SPL) is calculated using ANSYS Fluent 2021 R1's broadband noise model:

$$SPL = 20\log_{10}\left(\frac{p_{rms}}{p_{ref}}\right) \tag{16}$$

where p_{rms} is the root-mean-square acoustic pressure and $p_{ref} = 1 \times 10^{-6}Pa$.

2.2.3. Control equation of hydrofoil vortex-induced vibration

According to Newton's second law and Van der Pol's wake oscillator model, the motion governing equation of a hydrofoil for pitching motion in two dimensions with single degrees of freedom is as follows:

$$I_\alpha\ddot{\alpha} + C_\alpha\dot{\alpha} + K_\alpha\alpha = M \tag{17}$$

Where, I_α is the moment of inertia of hydrofoil; C_α is the damping coefficient of structure; K_α is the torsional stiffness coefficient of the structure; $\ddot{\alpha}$、$\dot{\alpha}$、α are angular acceleration, angular velocity and angle of torsional vibration, respectively. M is the external torque of hydrofoil.

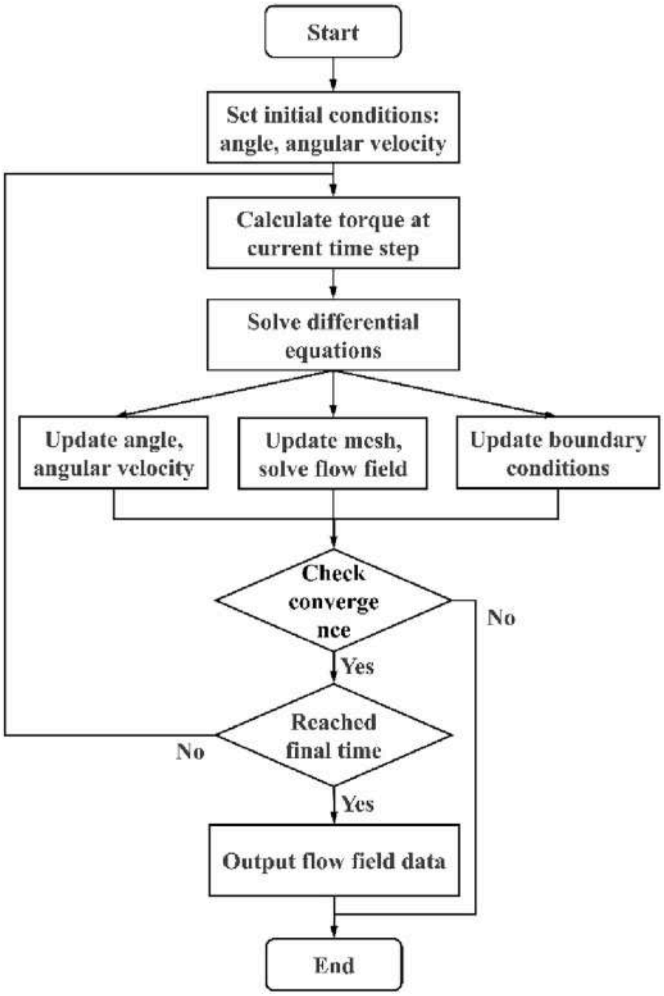

Fig. 2. Flow chart of numerical solution of vortex-induced vibration.

The moment of inertia I_α can be expressed as $I_\alpha = m{r_\alpha}^2 b^2$, where m is the mass of the hydrofoil, r_α is the radius of rotation around the center of rotation, the dimensionless quantity, and b is the length of half a chord. Mass ratio $m^* = m/\pi\rho b^2$, where ρ is fluid density.

Structure critical damping coefficient $C_0 = 2\sqrt{I_\alpha K_\alpha}$, dimensionless damping coefficient $\zeta = C_\alpha/C_0$, then the damping coefficient of hydrofoil can be expressed as $C_\alpha = 2\zeta\sqrt{I_\alpha K_\alpha}$, natural frequency $f_s = \sqrt{K_\alpha/I_\alpha}/2\pi$. Additionally, the two-dimensional single-degree-of-freedom hydrofoil's pitching motion governing equation can be expressed as follows:

$$\ddot{\alpha} + 2\zeta\omega_0\dot{\alpha} + \omega_0^2\alpha = M/I_\alpha \tag{18}$$

Where ω_0 is the circular frequency and the expression is $\omega_0 = 2\pi f_s$.

Equation (18) is discretized and solved using the fourth-order Runge-Kutta method. The angular velocity and angle corresponding to each time step are calculated to control the motion of hydrofoil and the updating of the mesh. The expressions of velocity $\dot{\alpha}_{(t_{n+1})}$ and $\alpha_{(t_{n+1})}$ obtained by discretization are shown in equations (19) and (20):

$$\dot{\alpha}_{(t_{n+1})} = \dot{\alpha}_{(t_n)} + \frac{\Delta t}{6} \times (K_1 + 2K_2 + 2K_3 + K_4) \tag{19}$$

$$\alpha_{(t_{n+1})} = \alpha_{(t_n)} + \Delta t \times \dot{\alpha}_{(t_n)} + \frac{(\Delta t)^2}{6} \times (K_1 + K_2 + K_3) \tag{20}$$

The expressions for K_1, K_2, K_3, and K_4 in the above equation are as follows:

$$K_1 = \frac{M}{I} - 2\zeta\omega_0\dot{\alpha}_{(t_n)} - \omega_0^2\alpha_{(t_n)} \tag{21}$$

$$K_2 = \frac{M}{I} - 2\zeta\omega_0\left(\dot{\alpha}_{(t_n)} + \frac{\Delta t}{2}\cdot K_1\right) - \omega_0^2\left(\alpha_{(t_n)} + \frac{\Delta t}{2}\cdot\dot{\alpha}_{(t_n)}\right) \tag{22}$$

$$K_3 = \frac{M}{I} - 2\zeta\omega_0\left(\dot{\alpha}_{(t_n)} + \frac{\Delta t}{2}\cdot K_2\right) - \omega_0^2\left(\alpha_{(t_n)} + \frac{\Delta t}{2}\cdot\dot{\alpha}_{(t_n)} + \frac{(\Delta t)^2}{4}\cdot K_1\right) \tag{23}$$

$$K_4 = \frac{M}{I} - 2\zeta\omega_0(\dot{\alpha}_{(t_n)} + \Delta t\cdot K_3) - \omega_0^2\left(\alpha_{(t_n)} + \Delta t\cdot\dot{\alpha}_{(t_n)} + \frac{(\Delta t)^2}{2}\cdot K_2\right) \tag{24}$$

Since it is calculated in the time domain, the initial conditions for given velocity and displacement are as follows:

$$\begin{aligned}\dot{\alpha}_{(t=0)} &= \dot{\alpha}_0\\ \alpha_{(t=0)} &= \alpha_0\end{aligned} \tag{25}$$

Fig. 2 presents the solution flowchart for unsteady simulation of a two-dimensional hydrofoil, incorporating a torsional vibration control program developed via UDF in ANSYS Fluent 2021 R1. The model is two-dimensional incompressible unsteady flow. The pressure-velocity coupled equation is solved using the COUPLED algorithm. A second-order upwind technique is used to discretize convective terms. A

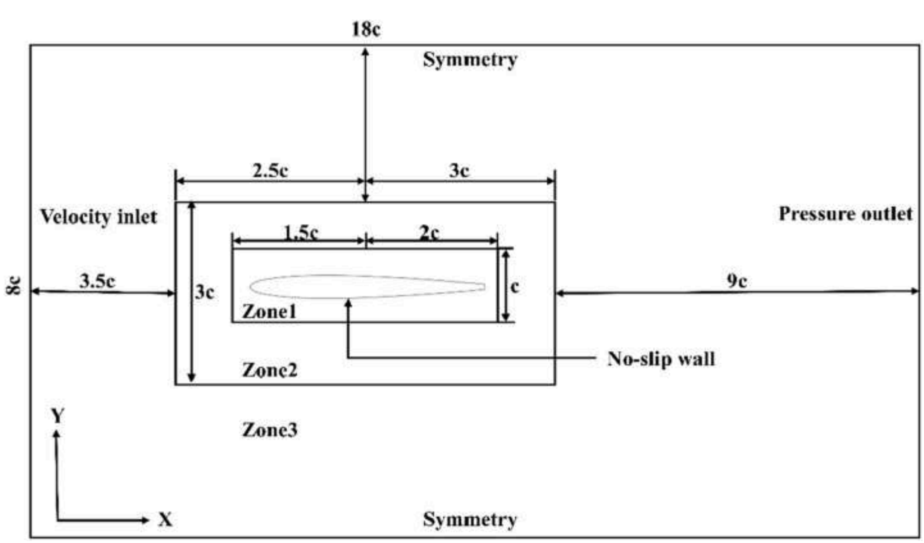

Fig. 3. Calculation domain and boundary conditions.

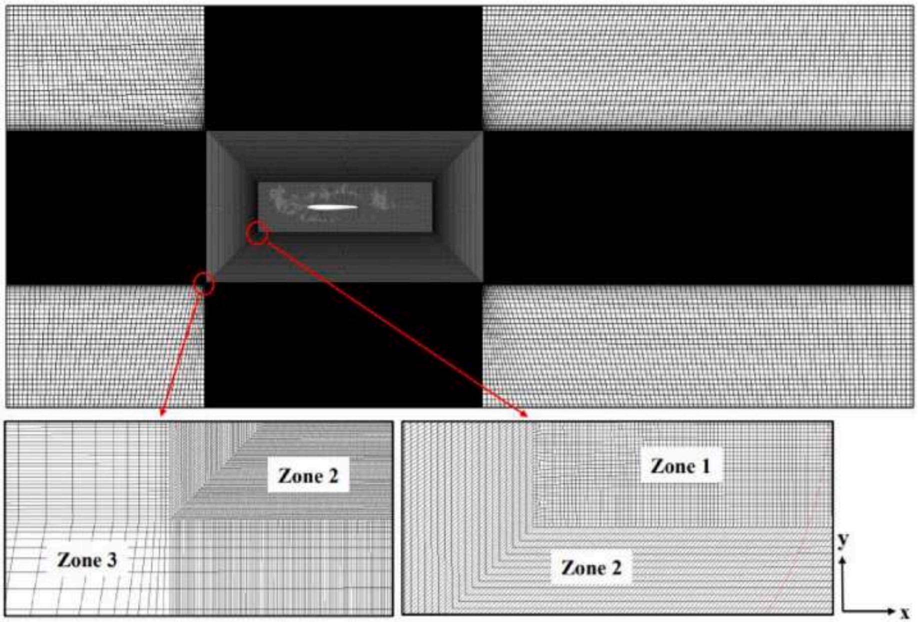

Fig. 4. Calculation domain grid.

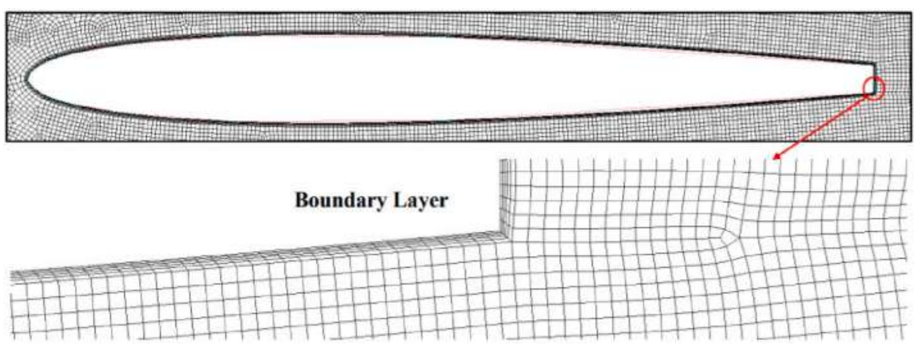

Fig. 5. Hydrofoil trailing edge area grid.

second order center discretizes the diffusion term. The gradient format is the least square method based on cell volume.

2.3. Computational domain and meshing

The boundary conditions of the hydrofoil pitch motion and the schematic diagram of the computational domain are displayed in Fig. 3. To avoid the boundary of the calculation domain affecting the simulation results, the computation domain's measurements along the x and y axes are $18c \times 8c$, respectively. The distance between the entrance of the calculation domain and the hydrofoil moving center is $6c$, and $4c$ is the distance between the hydrofoil movement center and the upper and lower borders. The symmetric boundary is the top and lower border of the computation domain, the hydrofoil boundary is the non-slip wall, the inlet boundary is the velocity inlet, and the outlet boundary is the pressure outlet. The graphic illustrates the division of the computing realm into three sections. During the simulation calculation, region 1 and hydrofoil move synchronously, while region 2 and region 3 remain stationary.

Structured quadrilateral grid is used to divide the calculation domain, which can accurately capture the flow field change and vortex shedding process around hydrofoil. The grid connections in various regions are connected by common nodes to guarantee computation accuracy. The grid division is shown in Fig. 4.

This research adopts the dynamic mesh model to simulate hydrofoil in the longitudinal direction of the single degree of freedom vibration. In the simulation, the region where the hydrofoil surface moves synchronously is defined as region 1 and the deformation region is defined as region 2. Region 2 uses a spring-based fairing technique to modify the moving boundary of region 1 by allowing the grid's internal nodes to move within the region. The overall number of nodes and connection ties don't vary, even though node placements might. To satisfy the boundary layer resolution requirements of the $SSTk-\omega$ turbulence model, the near-wall mesh of the hydrofoil is refined with a boundary layer configuration. The near-wall grid resolution is enhanced to $Y^+ \approx 1$, with the first-layer grid height set to $\Delta y = 5 \times 10^{-6} m$, validated using Equation (26). This approach facilitates detailed observation of flow field variations near the hydrofoil, while the mesh topology at the trailing edge is illustrated in Fig. 5.

$$Y^+ = \frac{u^* y}{\nu} \tag{26}$$

where u^* denotes the near-wall friction velocity, y represents the distance between the first-layer grid node and the wall surface, and ν is the kinematic viscosity of the fluid.

Table 1
Verification of grid number independence.

Grid number	$C_{m(\max)}$	f_{vs}
160012	0.0126	305.12
321050	0.0133	311.26
444890	0.0187	325.52
525515	0.0189	327.18

Table 2
Verification of time step independence.

$dt/\ s$	$C_{m(\max)}$	f_{vs}
3×10^{-5}	0.01862	327.31
2×10^{-5}	0.01864	325.62
1×10^{-5}	0.01865	325.52
5×10^{-6}	0.01867	322.76

3. Verification and validation

3.1. Grid and time step independence verification

The irrelevance is confirmed using the grid and time step of the fixed hydrofoil with attack angle 0° at inlet speed $U_r = 5.82$., and the moment coefficient C_m is defined as follows:

$$C_m = \frac{2M}{\rho U^2 c^2} \tag{27}$$

Four groups of grids with different grid resolutions are selected to verify the irrelevance of the number of grids: 160012, 321050, 444890, 525515, and the time step is set as $2\times 10^{-5}s$. Table 1 displays the computation results for various grid numbers. As the number of grids increases, the calculation results become closer and closer. For the case where the number of grids is 444890, further reducing the mesh size results in 1.070 % and 0.510 % changes in $C_{m(\max)}$ and f_{vs}, respectively. The results of numerical calculation are less affected by the number of grids, and the grids meet the requirement of independence.

The independence of the time step is verified on the basis of the number of grids being 444890. Four time steps from $5\times 10^{-6}s$ to $3\times 10^{-5}s$ are selected for verification, and the calculated results are shown in Table 2. The contrastive analysis found that from $1\times 10^{-5}s$ to $5\times 10^{-6}s$, the further reduction of time would make the change of $C_{m(\max)}$ and f_{vs} 0.107 % and 0.848 %.The results show that the time step has little effect on the numerical results and meets the requirement of irrelevance.

Based on the confirmation that the number of grids and the time step are independent, the number of grids is chosen as 444890 and the time step $1\times 10^{-5}s$ for the simulation calculation.

3.2. Verification of vortex shedding of fixed hydrofoil

As the fluid flows through the hydrofoil, a boundary layer is attached to the surface of the hydrofoil. A vortex that causes the boundary layer to alternately shed at the trailing edge under the action of a blunt trailing edge. The reference length h is the trailing edge's thickness, and the Strouhal number S_t is utilized in this study to describe the vortex shedding at the trailing edge. The Strouhal number is:

$$S_t = \frac{f_{vs} h}{U} \tag{28}$$

The time and frequency domain curves for the fixed hydrofoil's moment coefficients at flow velocity $U_r = 5.82$ are displayed in Fig. 6. The time domain curve is depicted in Fig. 6a; during the first stage, the vibration amplitude progressively increases while the moment coefficient is unstable. The hydrofoil wake is still developing at this point. The fluid domain stabilizes over time, and the curve begins to oscillate on a regular basis. At this time, periodic shedding vortices form behind the hydrofoil, and the wake vortex shedding mode is shown in Fig. 7. The frequency domain curve is obtained by Fourier transform of the data after the time domain curve is stabilized, as shown in Fig. 6b. The curve has a single peak with a frequency of 325.52Hz. Therefore, the oscillation frequency and vortex shedding frequency of the hydrofoil moment coefficient are both 325.52Hz. Strouhal number $S_t = 0.175$ is calculated according to equation (28).

The impact of advance speed $U_r = 5.82 \sim 8.73$ on the vortex shedding frequency is confirmed for hydrofoils with 0° angle of attack. By contrasting the numerical simulation findings with the simulation experiment results from the prior study, the accuracy of the simulation calculation approach is confirmed. The vortex shedding frequency simulation and experimental measurements at various flow rates are displayed in Fig. 8. The simulation results of this research are compared with the experimental data and simulation results of Ausoni et al. (2006)

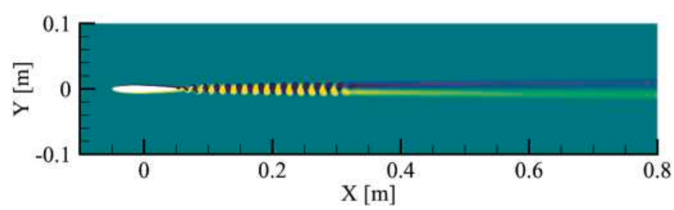

Fig. 7. Hydrofoil vortex shedding pattern at $U_r = 5.82$

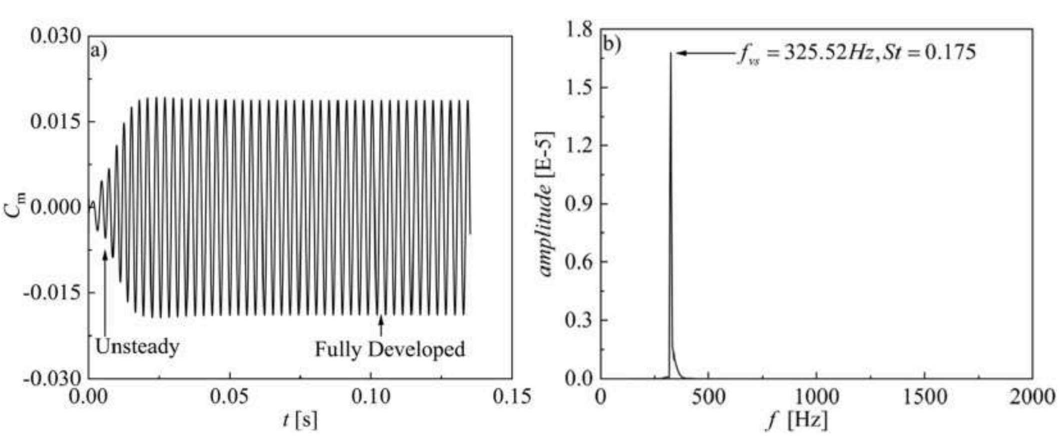

Fig. 6. Moment coefficient curve of hydrofoil at $U_r = 5.82$, a) Moment coefficient curve of time domain, b) Moment coefficient curve of frequency domain.

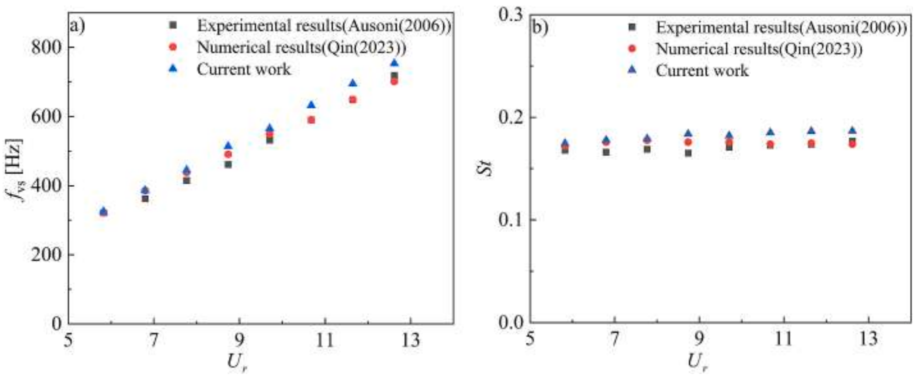

Fig. 8. Vortex shedding of the hydrofoil at the advance rate $U_r = 5.82 \sim 8.73$, a) Vortex shedding frequency at different velocity, b) *St* values at different flow rates.

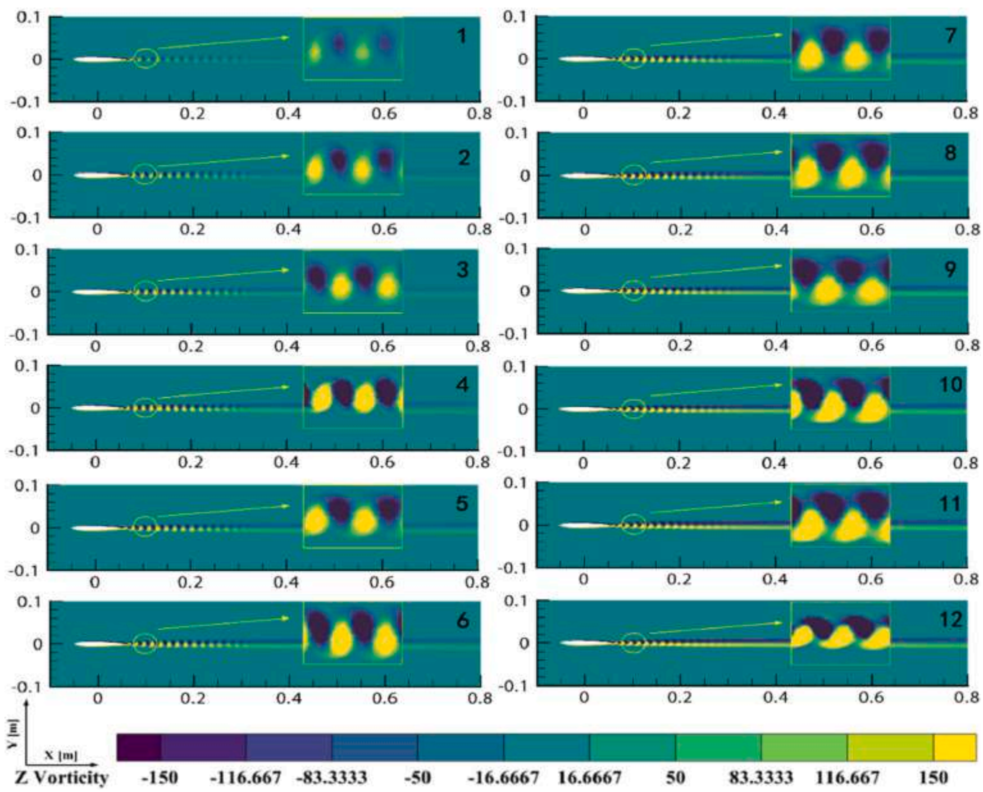

Fig. 9. Hydrofoil at reduced speed 1–12 vortex shedding condition.

and Qin et al. (2023a) in Fig. 8a. All of the simulation results in this work demonstrate a linear relationship between vortex shedding frequency and advance speed, and they are in agreement with the results of earlier experiments and simulations. Fig. 8b shows the relationship between Strouhal number S_t and advance speed, and the results show that S_t is independent of advance speed.

4. Simulation results of hydrofoil vortex-induced vibration

4.1. Simulation of hydrofoil vortex-induced vibration at different reduction velocities

By comparing and analyzing the torsive vibration of hydrofoil under different reduction speeds, the variation range of reduction speed is 1~12, and the corresponding Reynolds number increases from 3200 to 39000. Fig. 9 shows the vortex shedding behind the hydrofoil at different reduction speeds. It is discovered that the vortex alternatively falls off at the trailing edge and that the vortex-induced vibration takes place in the hydrofoil at varying reduction speeds. The difference lies in the length of the vortex wake and the alternation of the two rows of vortices in different rotation directions. When the reduced velocity reaches 4, a sudden change in the alternating vortex shedding spacing is observed, accompanied by an enlargement of the wake vortex. Notably, the spacing between counter-rotating vortices undergoes significant contraction. Furthermore, with progressive increase in reduced velocity, the vortex wake exhibits gradual elongation and enhanced distinctiveness. Vortices sharing identical rotational direction demonstrate increasing proximity, ultimately evolving into a well-defined vortex street configuration.

To further examine the hydrofoil's dynamic principle and ascertain the vortex shedding frequency, a velocity monitoring point is positioned at the back of the hydrofoil, as seen in Fig. 10. The principle of this arrangement is to directly measure transverse velocity fluctuations, which are the physical manifestation of the vortex shedding phenomenon. The choice to place monitoring points at the rear of the hydrofoil instead of directly measuring the hydrofoil lift fluctuations was a

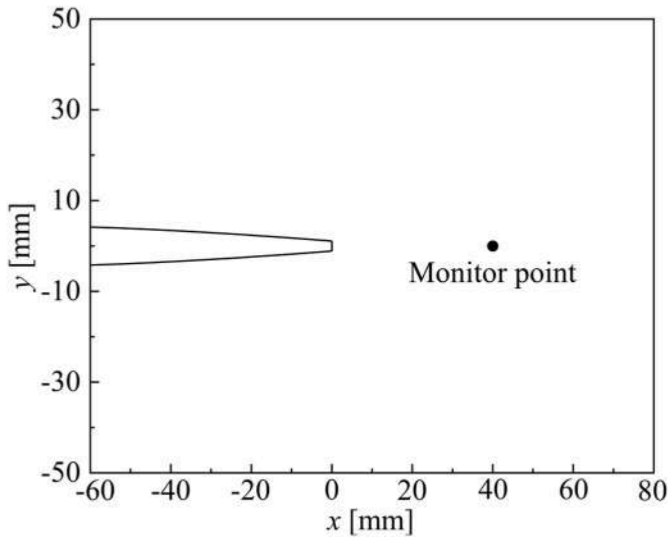

Fig. 10. Speed monitoring point behind hydrofoil.

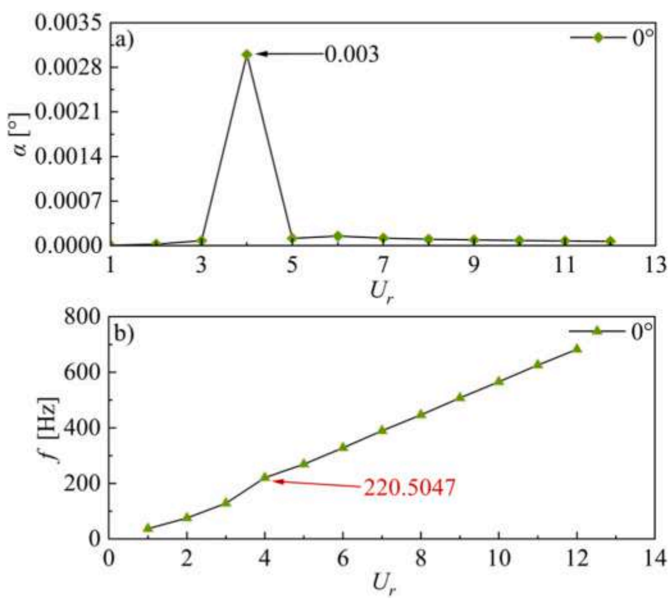

Fig. 11. Changes of hydrofoil torsional vibration angle and vortex shedding frequency under different reduction velocities, a) Torsional vibration angle, b) Vortex shedding frequency.

deliberate choice. When a hydrofoil's lift is measured, more drag is introduced, which could alter how frequently the hydrofoil experiences vortex shedding. On the contrary, a velocity monitoring point is set behind the hydrofoil to monitor the change of wake velocity when the hydrofoil falls off. Any fluctuations in speed here are attributed to the whirlpool from which the hydrofoil falls off, rather than an external force or vibration.

The direct correlation between transverse velocity fluctuations and vortex shedding frequency has been extensively validated in cylinder flow studies. Building upon this methodology, the present study identifies vortex shedding frequencies by monitoring lateral velocity components in the wake region. As established by Green and Gerrard (1993), the wake velocity field exhibits periodic oscillations during vortex street formation, with their frequency matching the vortex shedding frequency. It is therefore imperative to position the monitoring point within the fully developed vortex street region, typically located 1–2 characteristic lengths downstream. In numerical simulation, the

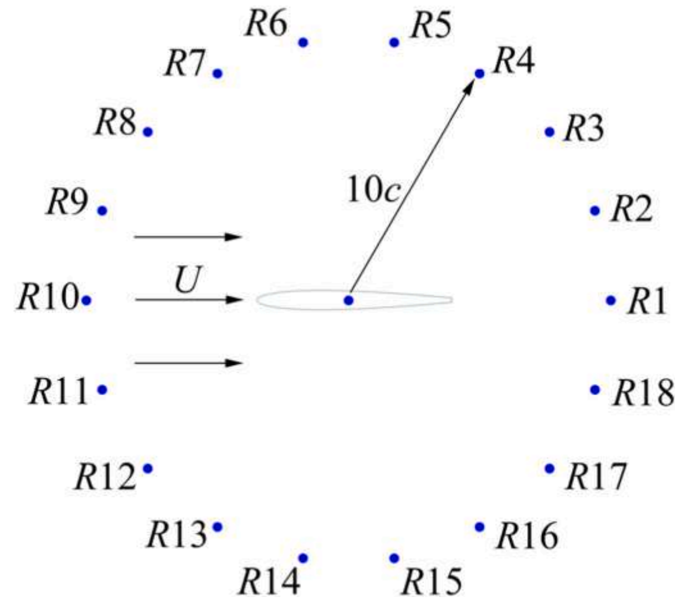

Fig. 12. Schematic diagram of the sound field around the hydrofoil.

monitoring point was placed 40 mm (approximately 1.5 chord lengths) aft of the hydrofoil, aligned with the canonical positioning for capturing fully developed vortex streets.

The torsional vibration angle variation and vortex shedding frequency of hydrofoil under different reduction speeds are shown in Fig. 11. As shown in Fig. 11a in the reduced rate of 4 when the maximum vibration amplitude. Vortex-induced resonance takes place at this moment when the hydrofoil's vortex shedding frequency is near to its natural frequency. The hydrofoil's vortex shedding frequency is 220.5047 Hz. Shown in Fig. 11b, because the vortex-induced resonance, the reduced speed 4 when mutated, changed the hydrofoil vortex distribution of the linear relationship between frequency and reduced speed.

In order to further analyze the noise changes around the hydrofoil under different reduction speeds, a circular sound field centered on the hydrofoil is established. The radius of the hydrofoil extends outward 10 times the chord length (10c) from the center. The primary monitoring point is located directly behind the hydrofoil and is designated R1. The subsequent points are arranged in a counterclockwise direction, with an angle of 20° between each point and the adjacent monitoring point, as shown in Fig. 12. In order to maintain consistency and comparability, the grid and time step for the sound field simulation are kept the same as the previous flow field simulation. This method ensures the consistency of simulation calculation and improves the effectiveness of comparative analysis.

Fig. 13 shows the integrated sound pressure level (SPL) direction diagram of the hydrofoil at different reduced velocities. In order to facilitate coherent comparative analysis, the data of SPL are represented in the form of polar graph. As shown in Fig. 13, the sound field exhibits dipole characteristics regardless of the flow rate of the hydrofoil. The variation of the SPL value on the horizontal axis is mainly affected by the drag, while the SPL along the vertical axis is related to the lift force exerted on the hydrofoil. As shown in Fig. 13, with the increase of reduction velocity, the flow field around the hydrofoil basically increases in equal proportion. Only when the reduced velocity is 4, the amplitude of hydrofoil increases abruptly due to vortex-induced resonance. The sound field around the hydrofoil also surges, and its sound field curve is between the reduced velocity 5 and 6. It is found that with the increase of reduced velocity, the vertical axial SPL value increases more than the horizontal axial value, indicating that the flow velocity has a greater effect on the lift force.

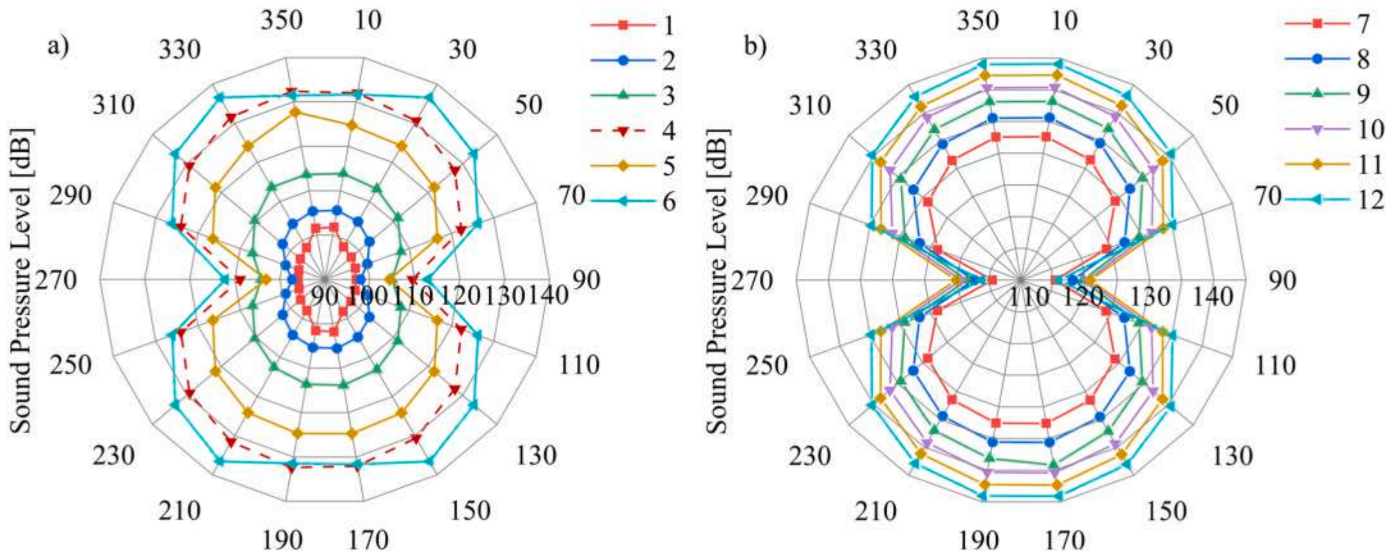

Fig. 13. Variation of sound field around hydrofoil at different reduced velocities, a) Reduced velocity 1–6, b) Reduced velocity 7-12.

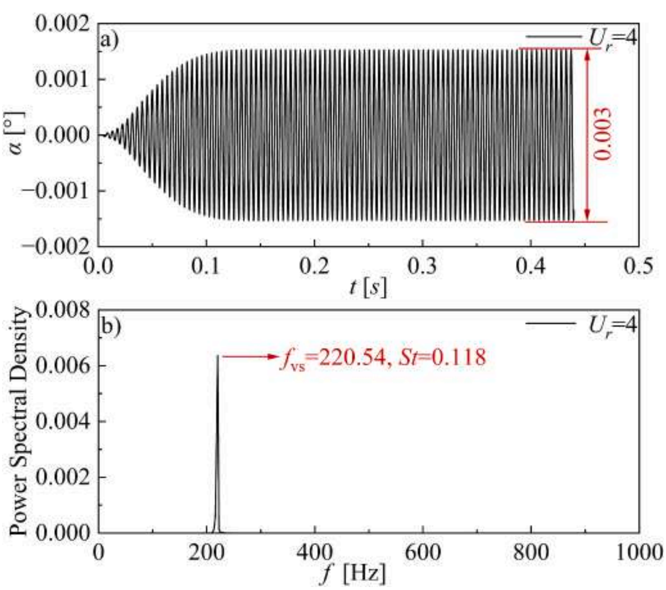

Fig. 14. Changes of hydrofoil torsional vibration angle and vortex shedding frequency when the reduced velocity is 4, a) Torsional vibration angle, b) Vortex shedding frequency.

Fig. 14 shows the changes of hydrofoil torsional vibration angle and vortex shedding frequency when the reduced velocity is 4. Fig. 14a shows the toroidal vibration angle change, and it can be seen that it is the same as the fixed hydrofoil, which also undergoes an unstable phase and a periodic oscillation phase. After stabilization, a periodic shedding vortex formed behind the hydrofoil. The hydrofoil moment coefficients are shown in Fig. 14b after Fourier transform. When the reduction velocity is 4, the hydrofoil's vortex shedding frequency is 220.54 Hz, and its Strouhal number, S_t, is 0.118.

At resonant and non-resonant flow rates, the pressure coefficient and sound pressure of hydrofoil are shown in Fig. 15, and the pressure coefficient C_p is defined as:

$$C_p = \frac{p_\infty - p}{\frac{1}{2}\rho V^2} \tag{29}$$

Where, p is the static pressure at a certain point on the surface of the hydrofoil, p_∞ is the far field static pressure, ρ is the water density, and V is the water flow velocity. In this case, the positive value of the pressure coefficient indicates the suction force.

According to Powell's vortex sound theory (Qian et al., 2025), the generation, evolution, and shedding processes of vortical structures in fluids directly induce acoustic pressure fluctuations. The resultant sound field can be interpreted as quadrupole radiation effects stemming from vorticity variations, whose intensity is intrinsically linked to the spatiotemporal distribution of vortices. During vortex-induced resonance of hydrofoils, the vortex shedding frequency locks in with the structural natural frequency, leading to significant intensification of periodic vortex shedding. This phenomenon exacerbates asymmetry in local flow pressure distributions and radiates acoustic energy through the fluid medium. Under resonant conditions, the synchronization between vortex shedding frequency and structural eigenfrequency results in reduced inter-vortex spacing and concentrated vorticity within the wake. As per vortex sound theory, such enhanced vortex interactions amplify quadrupole source intensity within the hydrodynamic-acoustic coupling mechanism. The pressure profiles at resonant and non-resonant flow rates are shown in Fig. 15a–c, and d. The surface pressure distribution of hydrofoil at non-resonant velocity is similar to that of fixed hydrofoil. Near the leading edge of hydrofoil, the pressure coefficient is more negative. At this time, the fluid flow rate decreases, resulting in the pressure at the leading edge being greater than the far-field pressure. Following that, the hydrofoil's surface pressure is essentially symmetrical. The flow rate of the fluid gradually increases, resulting in a gradual decline in the curve shown in Fig. 15a and a decrease in the hydrofoil surface pressure. As seen in Fig. 15d, truncation at the trailing edge causes the fluid velocity to drop and the pressure coefficient to rise suddenly. At this time, the hydrofoil vibration amplitude is small.

The pressure coefficient of the hydrofoil leading edge is also a large negative value at resonance velocity, which is the same as that at non-resonance velocity. Later, the hydrofoil's upper surface velocity rises, the pressure coefficient falls, the lower surface velocity falls, and the pressure rises as the torsional vibration angle grows. The hydrofoil's midway forms a symmetrical distribution of pressure, enclosing the hydrofoil's surface. The hydrofoil's torsional vibration angle will increase further when its upper left and lower right surface pressure coefficients are positive.

Fig. 15b shows how the maximum value of the integrated sound pressure level changes for both resonant and non-resonant flow rates in the sound field surrounding the hydrofoil. It is found that the resonance phenomenon makes the sound pressure rise in the frequency band below

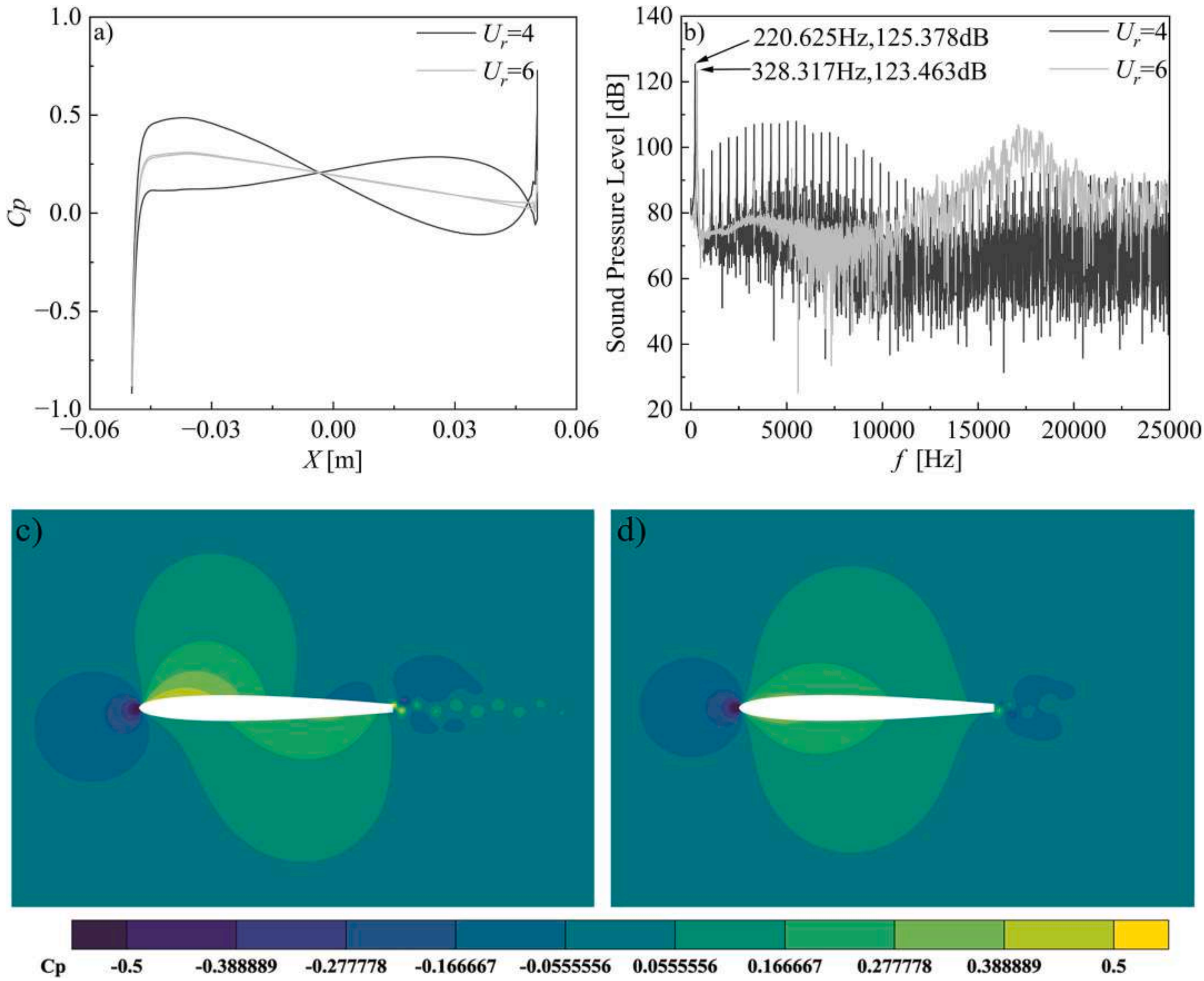

Fig. 15. Resonant and non-resonant flow velocity pressure coefficient and sound pressure changes, a) Pressure coefficient, b) Sound pressure changes, c) Cloud image of pressure coefficient at resonance velocity, d) Cloud image of pressure coefficient at non-resonant velocity.

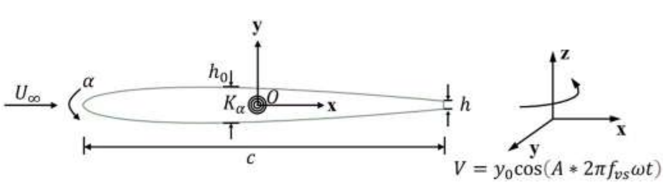

Fig. 16. Schematic of active open-loop control for hydrofoil torsional vibration.

12.5Hz. In the 12.5 kHz–20 kHz frequency range, the sound pressure is reduced due to resonance.

4.2. Actively control the vortex-induced vibration results of hydrofoil

This study employs User-Defined Functions (UDF) in ANSYS Fluent to implement vibration control of a hydrofoil. The DEFINE_CG_MOTION macro is utilized to define kinematic boundary conditions by assigning velocity and angular velocity parameters, enabling precise control of rigid-body motion. The position of moving boundaries is dynamically updated at each time step following iterative computations. Focused on resonance phenomena at a reduced velocity of 4, active control strategies are implemented in three degrees of freedom: translational motion along the X and Y directions, and rotational motion about the Z-axis (as illustrated in Fig. 16). A comparative analysis is conducted to evaluate control effectiveness under various excitation frequencies and amplitudes across different motion directions. The results demonstrate how systematic adjustment of control parameters influences vibration suppression performance, providing insights for optimal hydrodynamic control configuration. Excitation speed is defined as follows:

$$V = y_0 \cos(A * 2\pi f_{vs} \omega t) \tag{30}$$

Where, y_0 is the excitation amplitude and A is the excitation frequency doubling.

Fig. 17 shows the changes of the hydrofoil toroidal vibration angle and the mean value of sound pressure level after adjusting the amplitude of excitation velocity in X, Y and Z directions. As shown in Fig. 17a, the excitation amplitude in different directions has different effects on the torsional vibration angle of the hydrofoil. The change of excitation amplitude in X direction has the least effect on the torsional vibration of hydrofoil, while the change in Y direction has the most effect. When the amplitude of excitation velocity is 1, the torsional vibration angle of

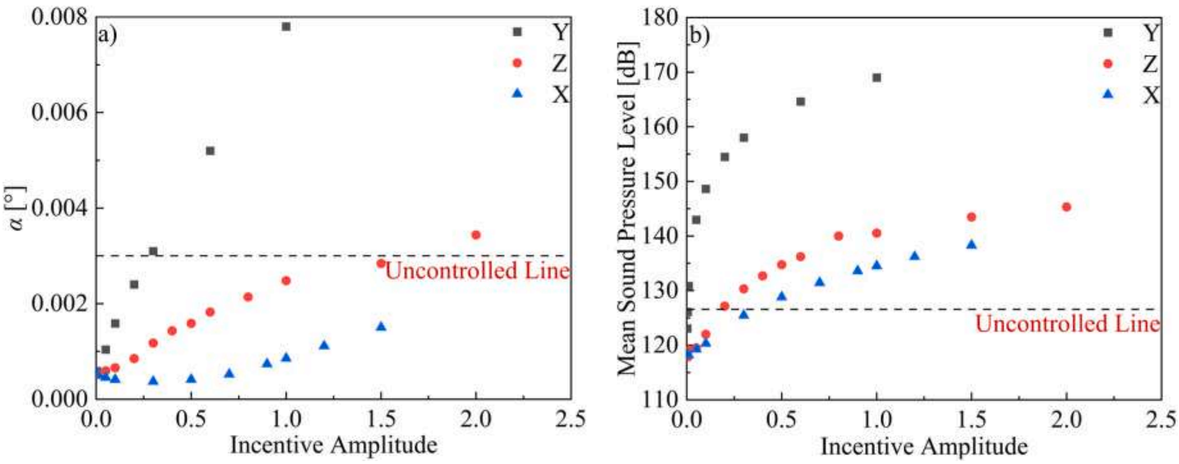

Fig. 17. Variation of toroidal vibration angle and average sound pressure level under different excitation amplitudes in different directions, a) Torsional vibration angle, b) Average sound pressure level.

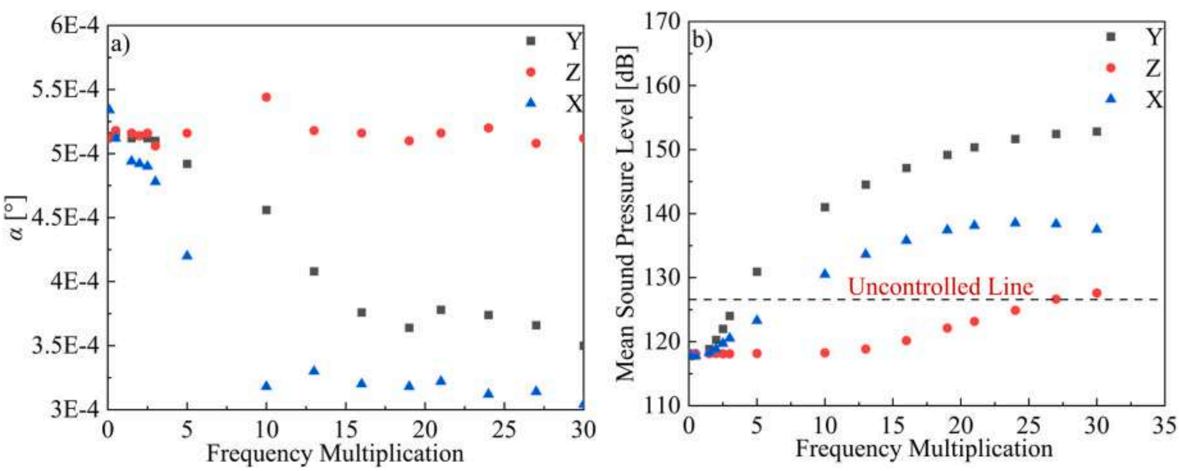

Fig. 18. Variation of toroidal vibration angle and average sound pressure level under different excitation frequencies in different directions, a) Torsional vibration angle, b) Average sound pressure level.

hydrofoil is twice of that before control. The mean change of sound field around hydrofoil after the control is applied is shown in Fig. 17b. The changes of excitation amplitudes in different directions have experienced a continuous development to a stable stage. Compared with the torsional vibration angle, the change of excitation amplitude has more influence on the mean sound pressure. The excitation amplitude decreased only in the range of 0∼0.5.

By comparing the control effects of different excitation amplitudes in

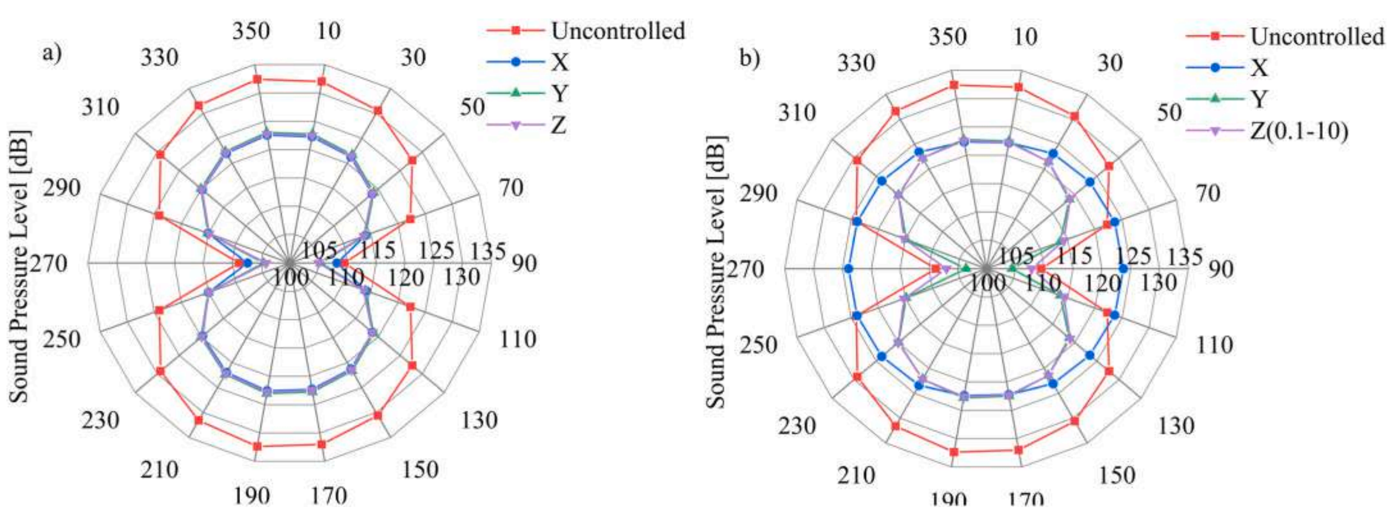

Fig. 19. Variation of sound pressure level of hydrofoil under different excitations in different directions, a) Amplitude of excitation, b) Frequency of excitation.

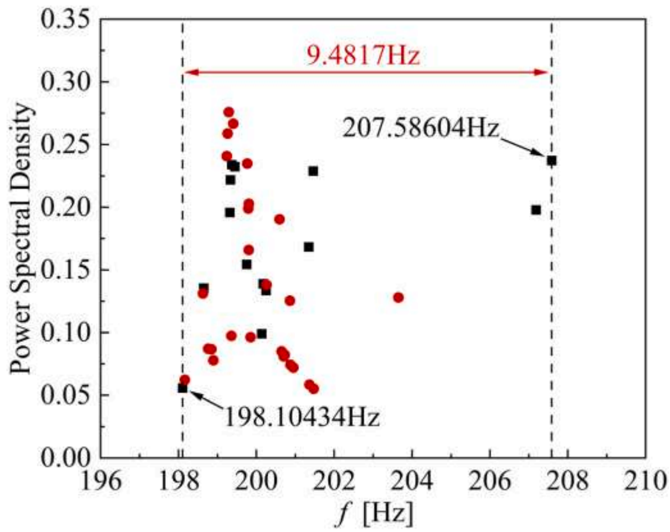

Fig. 20. Variation of hydrofoil vortex shedding frequency under multi-directional excitations.

different directions, the best control conditions of torsional vibration angle and mean sound pressure in each direction are selected. By adjusting the excitation frequency, the toroidal vibration angle of the hydrofoil and the change of the average sound pressure level are shown in Fig. 18. According to Fig. 18a, after changing the excitation frequency, the amplitude values of hydrofoil torsion are all reduced to 1/6 of those before control. The change of excitation frequency in Z direction has little effect on the change of torsional vibration angle. After adjusting the excitation frequency, the torsional vibration angle is always near $5.5E-4^{\circ}$. After the control is applied, the mean sound pressure around the hydrofoil changes as shown in Fig. 18b, which also goes through a stage of continuous development to stability. The influence of X and Y excitation frequencies on the mean sound pressure is great, and it only decreases at 0–5 times frequency. After changing the excitation frequency in Z direction, the mean sound pressure is smaller than the sound pressure before control, which has a good control effect.

According to Figs. 17 and 18, the working condition with the best control effect after changing the excitation amplitude and frequency in different directions is selected to compare and analyze the sound field around the hydrofoil. Fig. 19a shows the best control effect after changing the excitation amplitude in X, Y, and Z directions. The excitation amplitudes in different directions only affect the front and back ends of the hydrofoil. The control effect in the Z direction is the best, which is reduced by 5 dB compared to the control before. Fig. 19b shows the best control effect after adjusting the excitation frequency in three directions. After the excitation is applied in the X direction, the sound field no longer appears as a dipole. When the SPL value of the horizontal axis increases, the sound field appears as a circle. It can be seen that after changing the excitation frequency in X direction, the hydrofoil resistance increases and the lift decreases. In the Z direction, the sound field around the hydrofoil does not change when the excitation frequency is changed by 0.1–10 times, which has little effect on the lift resistance.

Fig. 20 shows the change of hydrofoil vortex shedding frequency when different excitation amplitudes and frequencies are applied in different directions, and the torsional vibration angle and sound field are reduced compared with those before the control. The frequency of hydrofoil vortex shedding is lower than it had been prior to control. The vortex shedding frequency is able to be dynamically changed by varying the excitation frequency and amplitude, and the bandwidth can be tuned to 9.4817 Hz.

The effects of different excitation frequencies and amplitudes on hydrofoil torsional vibration angle, mean sound pressure and direction of sound pressure level are analyzed comprehensively. The control effect is best when the excitation velocity amplitude is 0.0005 in the Y direction and the frequency doubling is 0.1.

According to equation (30), the pressure distribution around the hydrofoil with the best control effect is calculated and shown in Fig. 21. The trend of pressure distribution around the hydrofoil does not change before and after the control. The pressure distribution of flow field is similar to that of non-resonant velocity. After the control is applied in Y direction, the surface pressure of hydrofoil is basically symmetrical. The surface velocity of the hydrofoil increases, resulting in a tighter curve shown in Fig. 21a than before control. The symmetric distribution of surface pressure reduces the time interval of two vortices falling off in different directions at the trailing edge, and effectively controls the torsional amplitude of hydrofoil.

Fig. 22 shows the change after the control is applied in the Y direction. For the maximum SPL value of sound field before control, the noise is reduced by 5 dB at the emitted frequency of hydrofoil vortex. Within 20 kHz, the noise amplitude is effectively reduced. Similarly, the torque-vibration angle is reduced from 0.003° to 0.0005°, and the suppression rate is 83.3 %. The vortex shedding frequency of hydrofoil decreases from 220Hz before control to 199Hz, and the energy value decreases by 40.67 %. The observed post-control elevation in PSD levels originates from spectral redistribution of vortex shedding energy. Active control strategies suppress energy concentration near the dominant vortex shedding frequency (220 Hz) through modification of hydrofoil surface pressure distribution. Notably, while the primary sound pressure level (SPL) peak is reduced by 5 dB under control implementation, SPL augmentation emerges in higher frequency bands, manifesting characteristic energy transfer between control states. This spectral redistribution mechanism aligns with the frequency-domain modulation effects observed in cylindrical flow studies employing active flow control

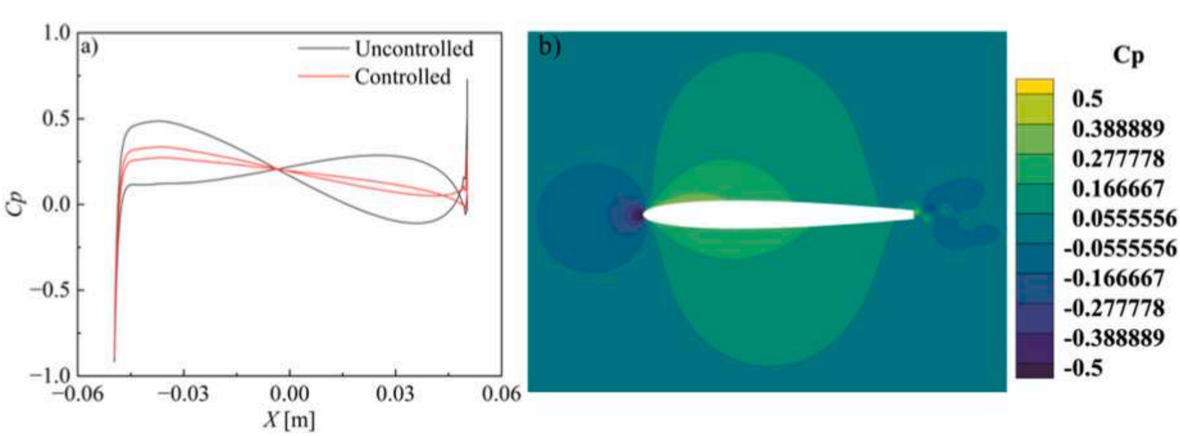

Fig. 21. Hydrofoil pressure coefficient diagram when the control effect is best, a) Pressure coefficient, b) Pressure coefficient cloud map.

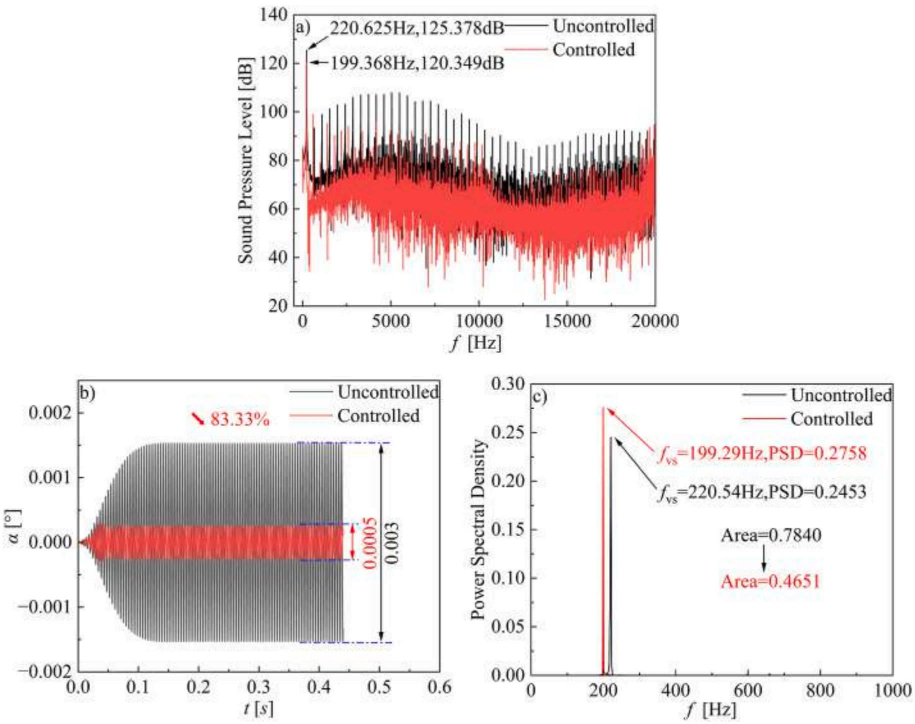

Fig. 22. Control effect is best when hydrofoil the loudest level, the angle and frequency of vortex distribution variation of torsional vibration, a) The loudest level, b) Torsional vibration angle, c) Vortex shedding frequency.

Fig. 23. Hydrofoil pasted with Macro Fiber Composite and its control schematic diagram.

(Bearman, 2003).

5. Experiment on active control of hydrofoil vortex shedding frequency

5.1. Hydrofoil vortex shedding frequency adjustment experiment device

The simulated item, a 3D printed NACA0009 hydrofoil with a blunt trailing edge, is identical to the experimental object. The material is PLA, and the surface is sprayed black. The vortex-induced vibration of hydrofoil is controlled by the d_{33} effect of Macro Fiber Composite (MFC). Apply epoxy adhesive to the surface of the hydrofoil, as shown in Fig. 23. The vortex shedding frequency of the hydrofoil is regulated by controlling the excitation frequency and voltage of MFC actuators, which induce chordwise vibrations along the polarization direction. To achieve precise modulation of near-wall flow characteristics, the MFC patches are bonded parallel to the chordwise direction on the upper surface trailing edge region of the hydrofoil (5 % chord length from the trailing edge), as illustrated in Fig. 23. The implementation comprises the following steps: (1) Surface preparation: The hydrofoil surface is abraded with 400-grit sandpaper to achieve a surface roughness Ra <1.6 μm, optimizing adhesive bonding strength. (2) Adhesive selection: A two-component epoxy resin (elastic modulus: 3.2 GPa) is selected to minimize interfacial stress concentration through modulus matching with the PLA substrate (elastic modulus: 2.5 GPa). (3) Curing protocol: Room-temperature curing is conducted for 24 h under 0.1 MPa applied pressure to eliminate air voids and ensure interfacial integrity. (4) Electrical interfacing: Electrodes are connected to an external power amplifier through flexible copper foil leads, maintaining mechanical compliance with the vibrating structure.

The active open-loop control strategy is implemented by driving the MFC actuators with sinusoidal voltage signals generated through a precision waveform generator (Agilent 33500B), thereby inducing periodic surface oscillations on the hydrofoil. The MFC model used in the test is COREMORROW M8557-P1, which can work at voltage from −500V to +500V. The actuating area is 85 × 57 mm, the maximum displacement is 153m, and the maximum output is 923N. It can fully satisfy the adjustment of the experimental excitation frequency and amplitude.

As seen in Fig. 24, the measurement device uses the particle image velocimetry (PIV) system RFlow-2d2c and the X150 high-speed camera from Qianyanlang Company to examine the vortex shedding behind the hydrofoil. The PIV system visualizes the flow field by capturing tiny particles scattered in the fluid (tracer particles) to build a vector diagram of the velocity field of the flow field (Kravtsova et al., 2014). During the experiments, polyamide (PSP) tracer particles (mean diameter: 10μm, density: 1.03g/cm^3) with density-matched characteristics (tracking fidelity error <1 %) were uniformly seeded into the flow field using a pneumatic atomizer. The particle mass concentration was maintained at 0.01 g/L through calibrated volumetric injection control.

The system employs a continuous-wave laser to uniformly illuminate tracer particles. A cylindrical lens assembly shapes the laser beam into a 1 mm-thick light sheet that covers the trailing edge region, ensuring full visualization of the hydrofoil wake zone. The high-speed camera and the particles' scattering toward the laser can record the particles' instantaneous displacement, creating a dynamic velocity field in real time. With a 5 megapixel (2560 x 1920) resolution, the X150 high-speed camera can capture stream fields at 2000 frames per second. The experimental

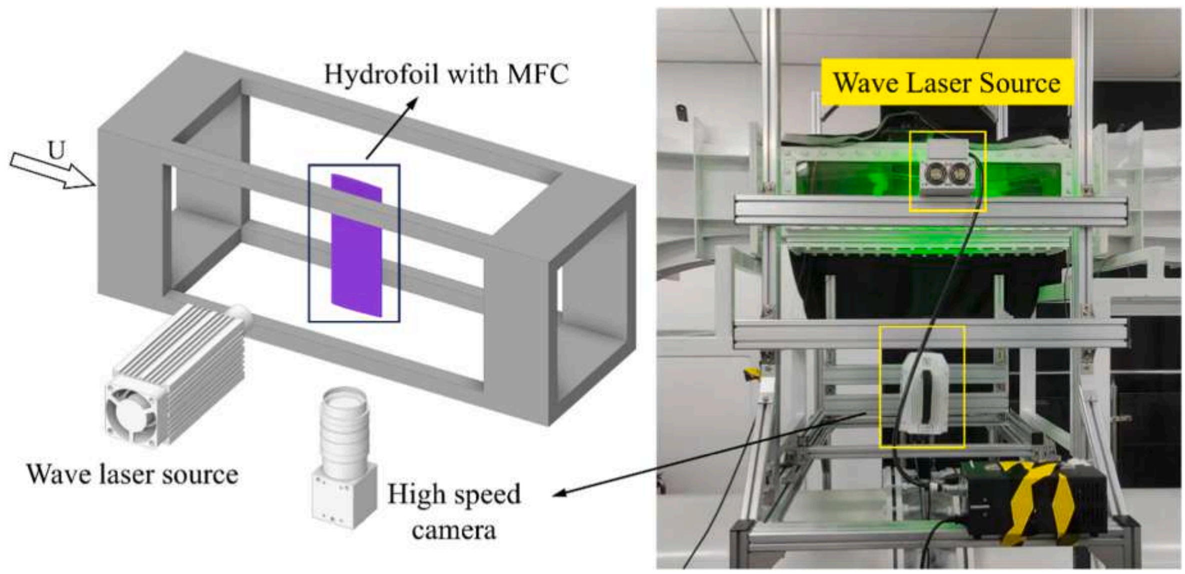

Fig. 24. Hydrofoil vortex-induced vibration active control device.

flow velocity range of $U_r = 0.097 \sim 0.97$ corresponds to vortex shedding frequencies of $f_s = 0 \sim 75Hz$. To achieve sufficient temporal resolution, the camera frame rate is maintained at 1000 times the instantaneous flow velocity, satisfying the Nyquist criterion (f < 0.5 × frame rate) for turbulence spectral analysis as prescribed by Markus Raffel et al. (2018). The high frame rate can precisely record the change

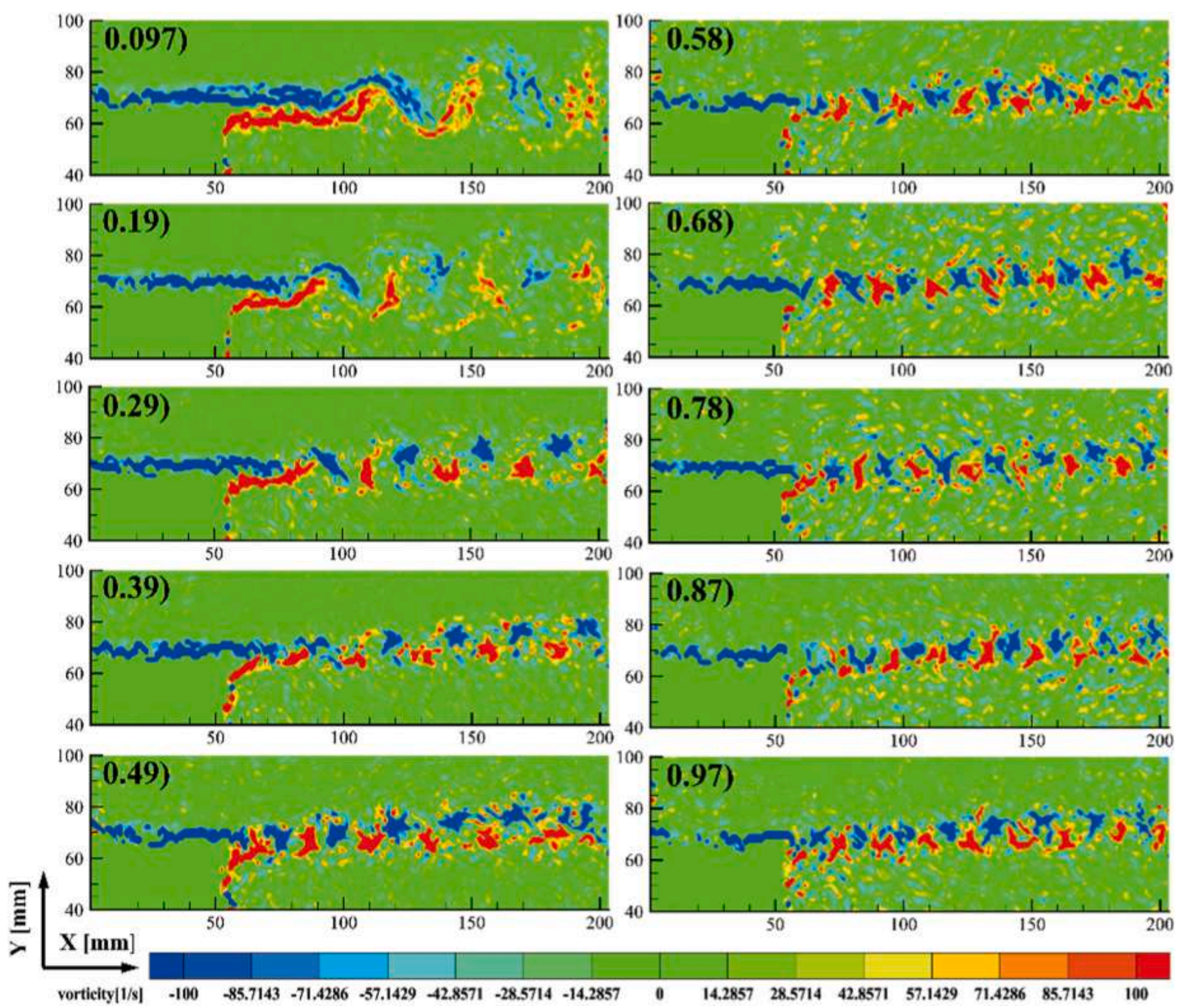

Fig. 25. Hydrofoil vortex shedding at different flow velocities.

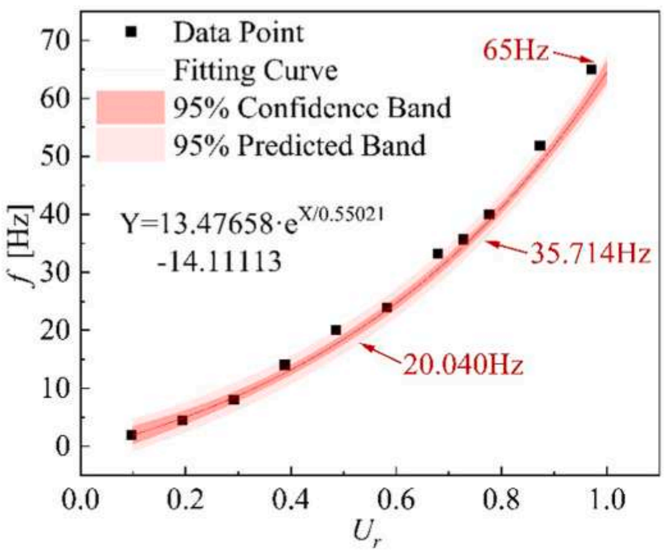

Fig. 26. Changes in the frequency of hydrofoil vortex shedding at different flow velocities.

in the flow field surrounding the hydrofoil and catch the fleeting process of vortex shedding.

The acquired particle image pairs are processed using an image cross-correlation algorithm with 64 × 64 pixel interrogation windows at 75 % overlap ratio. Velocity vector fields are derived from particle displacement tracking between consecutive frames, with computational accuracy enhanced through incremental window offset and multi-pass cross-correlation techniques. This yields a final vector grid resolution of 1.2 mm/vector, exhibiting measurement uncertainty below 0.1 pixel displacement (equivalent to velocity error ±0.02 m/s).

The uncertainties in the experimental process are systematically analyzed. The tracing fidelity of particles is evaluated using the Stokes number (St), where the particle relaxation time remains significantly smaller than the characteristic flow time scale, confirming their precise tracking capability for flow field variations (Markus Raffel et al., 2018). Image matching errors are controlled through calibration targets (±0.01 mm precision) and a multi-step cross-correlation algorithm, achieving displacement resolution better than 0.1 pixel with corresponding velocity uncertainty of ±0.02 m/s. Three sets of transient images are captured for each test condition to ensure stable development of flow structures. These analyses demonstrate that the experimental data reliability meets the requirements for vortex dynamic characteristics investigation.

5.2. Experimental results of active control of hydrofoil vortex shedding frequency

To comparatively analyze vortex-induced vibrations and trailing-edge vortex shedding characteristics of hydrofoils under varying flow velocities, PIV experiments are conducted on hydrofoils at reduced velocities ranging from 0.097 to 0.97. Active flow control is implemented by introducing external energy to disrupt the natural periodicity of vortex shedding, where MFC actuation generates micro-amplitude vibrations on the hydrofoil surface, thereby perturbing the boundary layer separation points and delaying the formation of dominant vortices.

The vortex shedding at the hydrofoil's trailing edge at varying flow rates is depicted in Fig. 25. It is evident that alternating falling vortices emerge at the hydrofoil's trailing edge at varying flow velocities. The size of the vortex and the frequency of vortex shedding are different. The vortex at the hydrofoil's trailing edge gradually shrinks, the two vortices in opposite directions gradually split apart, and the frequency of alternating shedding steadily rises as the flow velocity increases.

A velocity monitoring point is positioned 40 mm behind the hydrofoil to identify velocity variations at various flow rates in order to further examine the vortex shedding at the hydrofoil's trailing edge, as shown in Fig. 10. Fig. 26 illustrates how the vortex discharge frequency at the hydrofoil's trailing edge varies with flow velocity using the Fourier transform. It can be seen that the vortex emitting frequency of hydrofoil increases rapidly and exponentially with the increase of velocity.

The variation of hydrofoil vortex shedding frequency after adjusting MFC excitation frequency and amplitude at different flow velocities is shown in Fig. 27. The vortex shedding frequency at the hydrofoil's trailing edge changes when the flow velocity is at $U_r = 0.49$, excitation amplitude $3 \sim 7V$ and frequency $10 \sim 30Hz$ are altered, and when the flow rate is $U_r = 0.97$, excitation amplitude $3 \sim 7V$ and frequency $50 \sim 75Hz$ are adjusted, as seen in Fig. 27a and b.

By varying the stimulation frequency and amplitude, it is possible to actively modify the shedding frequency of the hydrofoil vortex, according to comparative analysis. The adjustment range of $U_r = 0.49$ is $10Hz$, and the adjustment range of $U_r = 0.97$ is $17.5Hz$. Different excitation amplitudes have different adjustable ranges. Under two flow rates, when the excitation amplitude is $3V$ and $5V$, only the vortex shedding frequency can be negatively adjusted. At $U_r = 0.49$, the vortex discharge frequency can be adjusted to $-7.5Hz$ before the control, and at $U_r = 0.97$, it is $-10Hz$. When the excitation amplitude is $7V$, the vortex shedding frequency can be adjusted positively and the vortex shedding can be accelerated. At $U_r = 0.49$, it can be adjusted to $+2.5Hz$ before control, and at $U_r = 0.97$, $+7.5Hz$. Moreover, by comparing the regions where the vortex shedding frequency varies with different excitation, it is found that there are more dots in the negative regulation region. It can

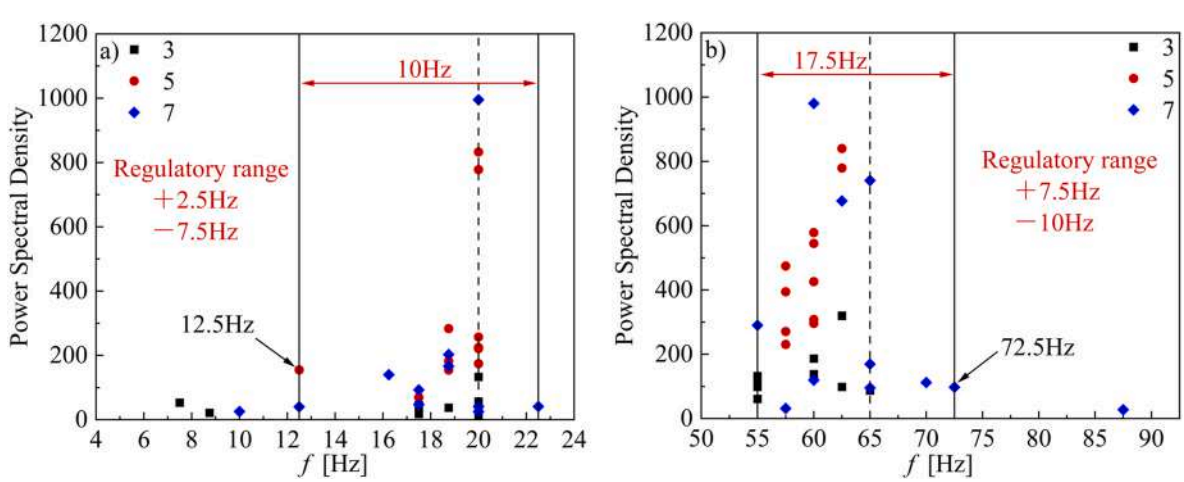

Fig. 27. Active control of hydrofoil vortex shedding frequency at different flow velocities, a) $U_r = 0.49$, b) $U_r = 0.97$

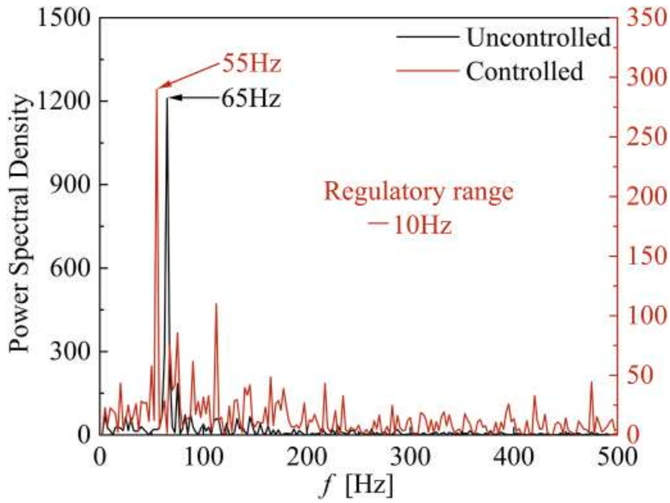

Fig. 28. Changes in the frequency of hydrofoil vortex shedding under active regulation.

be seen that the positive adjustment of vortex emission frequency is difficult. In comparison with the numerical simulation results of active torsional vibration control for hydrofoils presented in section 4.2, this study successfully achieved bandwidth adjustment ranges of 9.48 Hz and 17.5 Hz respectively. Both cases demonstrated effective active modulation of the hydrofoil's structural acoustic signature, thereby proposing a novel engineering application solution for active acoustic signature control of marine structures.

The change in vortex shedding frequency at the hydrofoil's trailing edge with a flow rate of $U_r = 0.97$, an excitation amplitude of $7V$, and a frequency of $55Hz$ is depicted in Fig. 28. The vortex shedding frequency is seen to drop from $65Hz$ prior to control to $55Hz$, which is in line with the excitation frequency. The active control modifies the hydrofoil surface's pressure coefficient distribution, modifies the surface vortex's shedding frequency, and successfully lowers the PSD value. The active control strategy was employed to verify the tunability of the vortex shedding frequency in hydrofoils and its regulatory capability on structural-acoustic characteristics. While the trailing-edge vortex shedding frequency decreased post-control, the introduction of external excitation induced energy redistribution in the frequency domain, leading to elevated power spectral density (PSD) levels. The trade-off between reduced vortex shedding frequency and increased local PSD values exhibits limited implications for engineering applications, as the associated negative impacts can be mitigated by the following critical factors: (1) Resonance Avoidance: When the dominant vortex shedding frequency approaches the structural natural frequency, resonance-induced fatigue damage becomes a significant risk. The active control strategy successfully reduced the shedding frequency from 220 Hz to 199 Hz, shifting it away from the natural frequency and substantially lowering resonance potential. (2) Validation Framework: The active modulation capability was rigorously verified through coupled numerical simulations and experimental investigations, establishing a robust foundation for engineering implementation.

The change in vortex shedding at the hydrofoil's trailing edge before

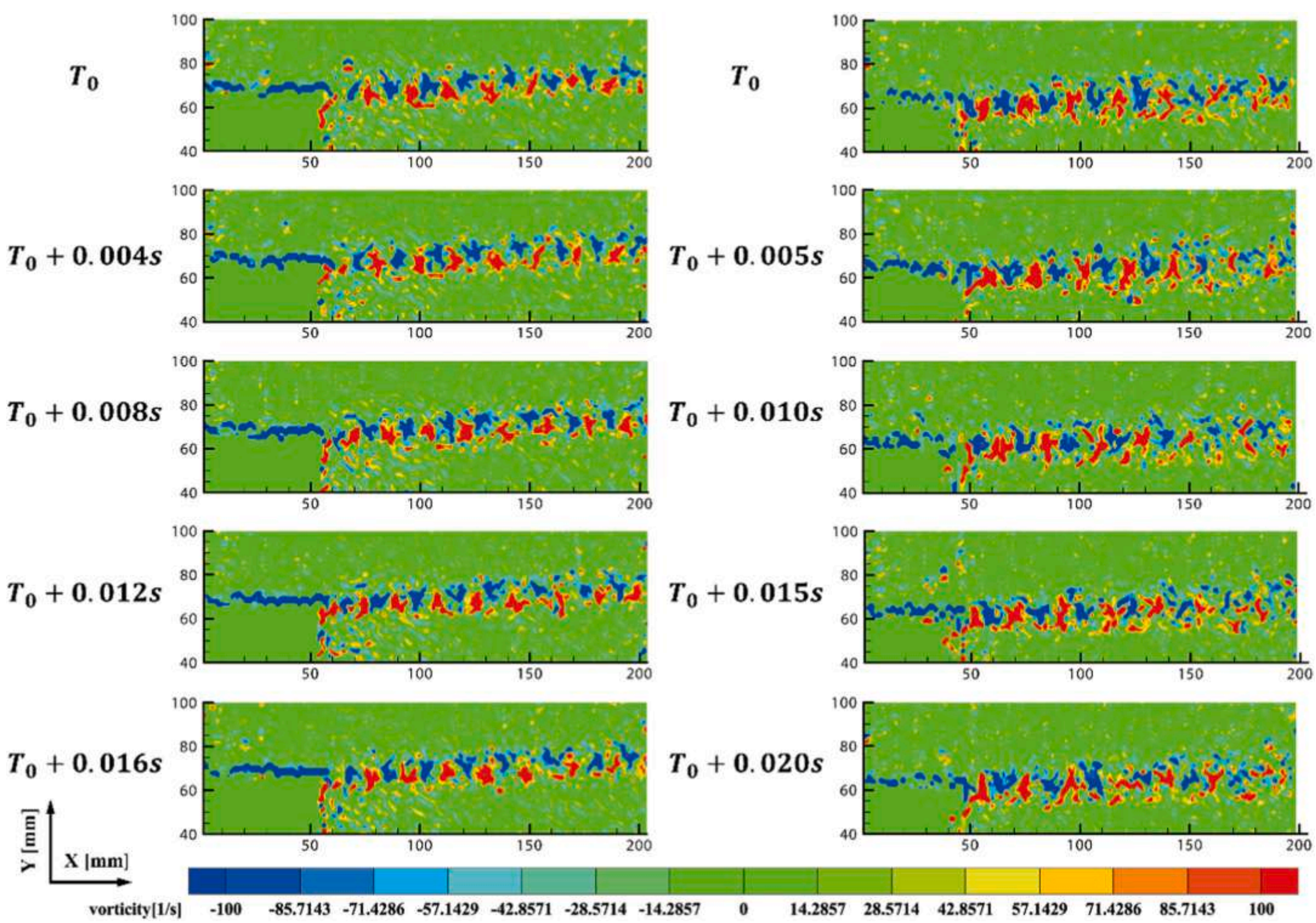

Fig. 29. Changes of hydrofoil vortex shedding under active control.

and after the control is depicted in Fig. 29. On the left, before control, the vortex discharge period is 0.016*s*. After the control is applied, its period is extended to 0.02*s*. The two rows of vortices pointing in separate directions are closer together once the hydrofoil's trailing edge has been controlled. In the similar observation range, the control vortex began to dissipate at about 200 mm, and the length of the two columns of vortices decreased, which directly verified the change of PSD value.

6. Conclusion

A two-dimensional hydrofoil torsional vibration simulation model is established based on the wake oscillator model. The vortex-induced vibration characteristics and active vibration control of hydrofoil at different flow velocities are systematically studied, and the following conclusions are mainly obtained.

(1) When the reduced velocity reaches 4, the wake shape, vortex shedding frequency, and sound pressure level all change, the hydrofoil torsional vibration angle increases suddenly, and the vortex shedding frequency approaches the natural frequency, causing vortex-induced resonance.
(2) There are differences in the distribution of resonant and non-resonant pressure coefficients. Resonance changes the symmetrical distribution of hydrofoil surface pressure, effectively reducing the torsional vibration angle of hydrofoil and the noise below 12.5 kHz.
(3) Varying excitation amplitude and frequency in different directions has different control effects. The control effect is best when the excitation velocity amplitude in the Y direction is 0.0005 and the frequency doubling is 0.1. The noise is reduced by 5 dB and the torsional vibration angle is reduced by 83.3 %.
(4) By adjusting the excitation frequency and amplitude, the hydrofoil vortex shedding frequency is actively adjusted, and the adjustable bandwidth is 9.4817Hz.

This study proposes an active control strategy for vortex shedding regulation in hydrofoil vortex-induced vibrations using Macro-Fiber Composite (MFC) actuators, offering a novel approach for acoustic signature manipulation of underwater structures. The flow field characteristics were experimentally investigated through Particle Image Velocimetry (PIV) measurements, enabling quantitative analysis of vortex shedding frequency variations under different control conditions. The following conclusions are reached.

(1) With the continuous increase of fluid velocity, the vortex shedding frequency of hydrofoil increases rapidly and exponentially.
(2) By comparing the changes of hydrofoil vortex shedding frequency under different excitations, the maximum active adjustment of 17.5Hz bandwidth can be achieved, and the number of points in the negative adjustment area is large.

CRediT authorship contribution statement

Jinliang Wu: Writing – review & editing, Writing – original draft, Visualization, Investigation, Formal analysis, Conceptualization. **Pengxiang Zhao:** Writing – review & editing, Investigation, Data curation. **Xin Lan:** Writing – review & editing, Validation, Methodology, Data curation. **Jinsong Leng:** Writing – review & editing, Investigation, Conceptualization. **Yanju Liu:** Writing – review & editing, Investigation, Conceptualization.

Declaration of competing interest

We declare that we do not have any commercial or associative interest that represents a conflict of interest in connection with the work submitted.

Acknowledgment

The authors wish to acknowledge the support given by the National Natural Science Foundation of China [Grant no.12072094 and 12272113].

References

Ausoni, P., Farhat, M., Bouziad, Y.A., Kueny, J.L., Avellan, F., 2006. Kármán vortex shedding in the wake of a 2D hydrofoil: measurement and numerical simulation. IAHR Int. Meeting of WG on Cavitation and Dynamic Problems in Hydraulic Machinery and Systems.
Bearman, P.W., 2003. Vortex shedding from oscillating bluff bodies. Annu. Rev. Fluid Mech. 16 (1), 195–222.
Caverly, R.J., Li, C., Chae, E.J., Forbes, J.R., Young, Y.L., 2016. Modeling and control of flow-induced vibrations of a flexible hydrofoil in viscous flow. Smart Mater. Struct. 25 (6), 065007.
Cheng, L., Z, Y., Zhang, M.M., 2003. Perturbed interaction between vortex shedding and induced vibration. J. Fluid Struct. 17, 2003.
Dongyang, C., Rui, X., Yaochen, L., Nansha, G., Guang, P., Marzocca, P., 2023a. Nonlinear energy sink-based study on vortex-induced vibration and control of foil-cylinder coupled structure. Ocean Eng. 286 (P2).
Dongyang, C., Rui, X., Zhida, Y., Guang, P., Pier, M., 2023b. The effect of vortex induced vibrating cylinders on airfoil aerodynamics. Appl. Math. Model. 115, 868–885.
Ducoin, A., Astolfi, J.A., Gobert, M.L., 2012. An experimental study of boundary-layer transition induced vibrations on a hydrofoil. J. Fluid Struct. 32 (none), 37–51.
Feng, C.C.B.S., 1968. The Measurement of vortex-induced Effects on Flow past Stationary and Oscillating Circular D-section Cylinders. National Taiwan University.
Green, R.B., Gerrard, J.H., 1993. Vorticity measurements in the near wake of a circular-cylinder at low Reynolds-numbers. J. Fluid Mech. 246, 675–691.
Griffin, O.M., 1995. A note bluff-body vortex formation. J. Fluid Mech. 284, 217–224.
Hartmann, A., Klaas, M., Schroeder, W., 2013. Coupled airfoil heave/pitch oscillations at buffet flow. AIAA J. 51 (7), 1542–1552.
Hasheminejad, S.M., Masoumi, Y., 2022. Hybrid active flow induced vibration control of a circular cylinder equipped with a wake-mounted smart piezoelectric bimorph splitter plate. J. Fluid Struct. 110, 103531.
Hu, J., Ning, X., Sun, S., Li, F., Ma, J., Zhang, W., 2022. Fluid-structure coupled analysis of flow-induced vibrations in three dimensional elastic hydrofoils. Mar. Struct. 84, 103220.
Kamrass, Joshua D., Thomas, Jeffrey, P., Tang, Deman, Besem, Fanny, 2016. Vortex-induced vibration and frequency lock-in of an airfoil at high angles of attack. J. Fluids Eng. Trans. Asme.
Kang, W., Liang, Q., Zhou, L., Wang, Z., 2022. Numerical investigation on torsional mode self-excited vibration of guide vane in a reversible pump-turbine during pump mode's starting up. J. Appl. Fluid Mech. 15 (6), 1789–1799.
Khalak, A., Williamson, C.H.K., 1999. Motions, forces and mode transitions in vortex-induced vibrations at low mass-damping. J. Fluid Struct. 13 (7–8), 813–851.
Kim, T., Hur, J., Lee, H., 2020. Numerical and experimental analysis of a singing propeller having blunt trailing edges. J. Ship Res. 64 (3), 234–249.
Kravtsova, A.Y., Markovich, D.M., Pervunin, K.S., Timoshevskiy, M.V., Hanjalic, K., 2014. High-speed visualization and PIV measurements of cavitating flows around a semi-circular leading-edge flat plate and NACA0015 hydrofoil. Int. J. Multiphas. Flow 60, 119–134.
Lee, A.J., Suk Suh, H., Jeon, C.-H., Kim, S.-G., 2016. Effects of one directional pneumatic tube system on routine hematology and chemistry parameters; A validation study at a tertiary care hospital. Practical laboratory med. 9, 12–17.
Markus Raffel, E., Willert, C., Scarano, Fulvio, J, Kähler, C., Wereley, T., S, Jürgen Kompenhans, 2018. Particle Image Velocimetry. Springer, Cham.
Mehmood, A., Abdelkefi, A., Akhtar, I., Nayfeh, A., Nuhait, A., Hajj, M., 2012. Linear and nonlinear active feedback controls for vortex-induced vibrations of circular cylinders. J. Vib. Control 20 (8), 1137–1147.
Muddada, S., Patnaik, B.S.V., 2010. An active flow control strategy for the suppression of vortex structures behind a circular cylinder. Eur. J. Mech. B Fluid 29 (2), 93–104.
Ni, Z., Dhanak, M., Su, T.C., 2019. Performance of a slotted hydrofoil operating close to a free surface over a range of angles of attack. Ocean Eng. 188, 6.
Qian, Z., Zeng, Y., Yao, Z., Wu, Q., Luo, X., 2025. Effect of leading-edge cavitation of a hydrofoil on the near-field sound pressure. Phys. Fluids 37 (1).
Qin, G., Zhang, H., Li, D., 2023. Numerical study on vortex induced vibration of hydrofoils with trailing-edge truncation. Ocean Eng. 275, 14.
Shigeki, K., Giwon, H., Naoto, M., Tomonori, Y., Shinobu, Y., 2018. Numerical study of active control by piezoelectric materials for fluid–structure interaction problems. J. Sound Vib. 435, 23–35.
Smith, S.M., Venning, J.A., Pearce, B.W., Young, Y.L., Brandner, P.A., 2020. The influence of fluid-structure interaction on cloud cavitation about a stiff hydrofoil. Part 1. J. Fluid Mech. 896, 35.
Smith, S.M., Brandner, P.A., Pearce, B.W., Venning, J.A., Clarke, D.B., 2021. Steady and unsteady loading on a hydrofoil immersed in a turbulent boundary layer. J. Fluid Struct. 102 (3), 103225.
Tian, J., Croaker, P., Li, J.S., Hua, H.X., 2017. Experimental and numerical studies on the flow-induced vibration of propeller blades under nonuniform inflow. J. Eng. Maritime Environ. 231 (2), 481–495.
Wang, Y., Cao, L.L., Zhao, G.S., Liang, N., Wu, R., Wu, D.Z., 2022. Experimental investigation of the effect of propeller characteristic parameters on propeller singing. Ocean Eng. 256, 15.

Williamson, C.H.K., Roshko, A., 1988. Vortex formation in the wake of an oscillating cylinder. J. Fluid Struct. 2 (4), 355–381.

Yarusevych, S., Boutilier, M.S.H., 2011. Vortex shedding of an airfoil at low reynolds numbers. AIAA J. 49 (10), 2221–2227.

Young, Y.L., Chang, J.C., Smith, S.M., Venning, J.A., Pearce, B.W., Brandner, P.A., 2022. The influence of fluid-structure interaction on cloud cavitation about a rigid and a flexible hydrofoil. Part 3. J. Fluid Mech. 934, 46.

Zhang, Y.K., Feng, Y.J., Chen, W.X., Gao, F., 2022. Effect of pivot location on the semi-active flapping hydrofoil propulsion for wave glider from wave energy extraction. Energy 255, 16.

Zhang, X., Chen, D., Luo, Y., Lin, Y., Liu, J., Pan, G., 2024a. Vortex-induced vibration characteristics of rigidly connected four-cylinder system and nonlinear energy sinks for vibration suppression. Phys. Fluids 36 (6).

Zhang, X., Chen, D., Tang, Y., Lin, Y., Liu, J., Pan, G., 2024b. Vortex-induced vibration and energy harvesting of cylinder system with nonlinear springs. Phys. Fluids 36 (10).

Zhao, P.X., Wu, J.L., Zhang, X.D., Lan, X., Leng, J.S., Liu, Y.J., 2024a. Numerical simulation of the vortex shedding and lock-in phenomenon of an active vibration hydrofoil. Ocean Eng. 309, 16.

Zhao, P.X., Zhang, X.D., Wu, J.L., Lan, X., Leng, J.S., Liu, Y.J., 2024b. Analysis and control of hydrofoil vortex-induced vibration. Ocean Eng. 313, 19.

Zobeiri, A., Ausoni, P., Avellan, F., Farhat, M., 2012. How oblique trailing edge of a hydrofoil reduces the vortex-induced vibration. J. Fluid Struct. 32, 78–89.